



UNIVERSITY OF AMSTERDAM



MSc Physics and Astronomy

Science for energy and sustainability

Master Thesis

Determining the resolution of coherent CL and characterization of optical materials

by

Joris Schefold

1042 1092

60 ECTS

September 2017 – June 2018 (10 months)

1st Examiner:

Prof. Dr. Albert Polman

Daily Supervisor:

Dr. Sophie Meuret

2nd Examiner:

Prof. Dr. Mark Golden



Center for Nanophotonics, AMOLF

Science Park 104, 1098 XG

Amsterdam, The Netherlands

TABLE OF CONTENTS

1	Introduction	4
1.1	Context.....	4
1.2	Outline.....	5
2	Resolution of coherent CL.....	6
2.1	Determining the resolution.....	6
2.2	System and sample	12
2.2.1	Sample preparation	12
2.2.2	Cube width	13
2.2.3	Beam diameter.....	14
2.3	The SE model	16
2.3.1	Concept	16
2.3.2	Mathematical model.....	16
2.3.3	Implementation	18
2.4	The CL model.....	19
2.4.1	Concept	19
2.4.2	Mathematical model.....	20
2.4.3	Implementation	21
2.4.4	MNPBEM17	22
2.5	Dealing with carbon contamination	24
2.5.1	Evidence of contamination	24
2.5.2	Filtering procedure.....	24
2.5.3	Robustness of procedure	26
2.5.4	Simplified model	27
2.6	Promises of a better precision	28
3	Discovering defects in a green LED	30
3.1	Introduction	30
3.2	Top view	31
3.3	Study of the side view of single Nanowire.....	34
3.4	EDX on horizontal NW.....	35
3.5	Conclusion.....	36
4	Grain boundary of degraded multi-crystalline Silicon solar cell	37
4.1	Introduction	37
4.2	Outline and experimental setup	37

4.3	Current-dependent regeneration test	39
4.4	Variation along the grain boundary	40
4.5	Variation perpendicular to the grain boundary	42
4.6	Conclusion	44
	Bibliography	46
	Acknowledgements	50

1 INTRODUCTION

1.1 CONTEXT

Technological advancements are often caused by finer control over materials properties and, as a result, the further miniaturization of devices. Ever since 1965, when Moore postulated his now famous law¹, computer chip performances have doubled every 18 months. Because of this, a modern smartphone has about the same computing power as the best supercomputers of 30 years ago². Besides driving the information explosion, more knowledge about and control over nanoscale fabrication processing also contributed to recent advancements in solar cell efficiency³⁻⁵, medicine^{6,7}, and lighting⁸.

Paramount to this progress is our ability to image nanoscale objects and investigate material properties on the atomic scale. Far-field optics is an incredibly useful tool for studying objects on the micrometre scale, but is, in the end, diffraction limited to about half the light wavelength. Because of this, only highly energetic photons, such as X-rays, can image a nanostructure. State of the art X-ray experiments have demonstrated a spatial resolution of 10 nm⁹ and reconstructed protein structures with 1.9 Å resolution^{10,11}. To achieve this sub-nanometre resolution, hundreds of large protein crystals were slowly rotated while being illuminated by femtosecond pulses of an X-ray free-electron laser. This way they could collect a diffraction pattern before the proteins were destroyed. Based on these patterns, a Monte-Carlo algorithm could then reconstruct the protein structure¹². Furthermore, two recent techniques have broken the diffraction limit, without using potentially sample destroying X-rays, by utilising fluorescent proteins^{13,14} for which they have been awarded the 2014 Nobel prize in chemistry. Nevertheless, the need for fluorescent molecules, and lack of spectral data, limits the potential of these techniques.

In the cases where the aforementioned techniques do not provide the desired spatial resolution, damage the sample too much, or are undesirable for other reasons, electron microscopy could be the right tool for the job. In an electron microscope, an electron is released from a heated tip and accelerated towards the sample. Depending on which electrons are subsequently collected electron microscopes are split into two groups. Scanning electron microscopes (SEM) accelerate electrons to 1-50 keV and use them to look at secondary electrons and sometimes backscattered electrons. In the (scanning) transmission electron microscope (STEM), the electron beam is generally in the 50-300 keV range and is used to look at samples of a couple tens of nanometers¹⁵. Besides a secondary electron detector, a STEM also has detectors after the sample that are used to look at the transmitted and scattered electrons. These electron microscopes can achieve nanometre resolution because the de Broglie wavelength of electrons, which determines their diffraction limit, is less than 0.1 Å for acceleration energies above 20 keV¹⁶. At this energy, the theoretical maximal resolution would thus be 0.05 Å and at higher energies, it would be even lower. The current record resolution is 40.5 pm which was achieved in a STEM at 300 keV¹⁷. Besides imaging nanostructures, we would also like to know their material properties such as their local chemical composition, optical properties, crystallographic structure etc. In an electron microscope there are three main techniques, shortly explained bellow, that yield (some of) this information while retaining their excellent spatial resolution, energy-dispersive X-ray spectroscopy (EDX), electron energy loss spectroscopy (EELS), and cathodoluminescence (CL).

EDX uses characteristic X-rays, emitted by the sample under irradiation, to determine its composition. These X-rays are emitted when a higher band electron recombines with a vacancy that was excited by

the electron/X-ray beam of the microscope. The energy of these X-rays depends on the atom from which it came and can thus be used to determine the chemical composition of a material. Recently, elemental EDX maps have been quantitatively analysed with atomic resolution¹⁸. EDX is used in chapter 2 to characterize a changing alloy concentration along the growth direction of a nanowire (NW).

In EELS the energy of a high-energy monochromatic (ΔE between 10 meV and 500 meV) electron beam is measured after interaction with a thin sample. By measuring the energy loss of electrons after interaction with the sample, information is obtained about the electronic band structure, plasmons, and chemical composition¹⁶. This technique has been used since 1944¹⁹, and it is claimed that it might also become diffraction limited in the near future, which would imply a <10 meV energy and atomic spatial resolution²⁰.

CL is another spectroscopy technique that is commonly used in electron microscopes and is the technique studied in the following thesis. It was first demonstrated in 1879 when Crookes observed light from phosphors that were irradiated by fast electrons²¹. However, it was not until the 1930-1960s, when SEMs became commercially available, that CL became more widely used. CL is generally divided into two classes, coherent and incoherent, depending on the interaction process responsible for the emitted light²². Incoherent CL is analogous to photoluminescence. In both, a charge carrier is excited and subsequently decays through a stochastic process which leads to the emission of a photon (luminescence). The main difference between PL and incoherent CL is that the electrons in incoherent CL can transfer more momentum than the photons of PL, which means that they couple more strongly to metastable levels. Furthermore, these fast electrons function as a supercontinuum source of light and thus do not allow the selection of which excitation is probed¹⁶. The second type of CL, coherent CL, can come from multiple processes that all have a fixed phase relation with the incoming electron and can be described using the Maxwell equations. While the origin of these processes is diverse, they all come from the interaction of the evanescent field of the electron with the sample. These processes include transition radiation, Cherenkov radiation, and diffraction radiation¹⁶. Furthermore, coherent CL can also be used to study surface plasmons²³.

1.2 OUTLINE

The second chapter of this thesis will be dedicated to determining the resolution of coherent CL. This will be done by scanning over a silver nanocube and recording an SE contrast and CL intensity at each pixel. By building two models, one for the SE and one for the CL signal, we then determine the location of the edges of the cube. By comparing how accurate and precise CL can match the SE data we then calculate the resolution. In chapter three, incoherent CL is used to determine the origin of two luminescent peaks in a Wurtzite $Al_{0.25}In_{0.75}P$ NW. EDX is subsequently used to link these two peaks to a gradient in the Al concentration. Incoherent CL is also used in chapter four to do a preliminary investigation into the influence of the grain boundary of a multi-crystalline silicon solar cell on the CL spectra as well as the optical effect of degradation.

2 RESOLUTION OF COHERENT CL

2.1 DETERMINING THE RESOLUTION

Metallic nanoparticles can confine light into regions smaller than the photon wavelength, due to the collective oscillations of free electrons at the surface of these nanoparticles, called surface plasmon modes²⁴. These nanoparticles can be used in a wide variety of systems such as amplifiers for lasers^{25,26}, computational systems where plasmons are used as information carrier instead of an electric signal²⁷⁻²⁹, or biosensing³⁰. To fully characterise these plasmonic nanostructures, a probe that is smaller than the optical diffraction limit is needed. Since electrons can be focused in a sub-nanometre probe, electron-based spectroscopy is ideally suited for the characterisation of these nanostructures¹⁶. The two main spectroscopy techniques used to investigate the plasmonic nature are Electron Energy Loss Spectroscopy (EELS)^{31,32} and Cathodoluminescence (CL)^{33,34}. Both probe the z-LDOS by studying the interaction between the evanescent electric field of the electron and the plasmon mode. This is done by focusing a fast electron beam close to, or on, the nanostructure. EELS then measures the energy spectrum of the electrons after interaction with the sample. Each loss peak in the energy spectrum corresponds to the strength of the modes at that energy¹⁶. Hereby, EELS yields information about both the bright and dark modes in thin samples³⁵. This is in contrast to CL, which only probes the radiative part of the z-LDOS³⁶ and works for a wider range of sample thicknesses. In CL a parabolic mirror collects the light that is emitted by the sample. This light can come from multiple processes which are generally classified into two categories, coherent and incoherent. Incoherent CL is caused by a stochastic process, such as electron hole recombination, which has no fixed phase relation between the phase of the incoming primary electron and the outgoing photon. This phase relation is present in coherent CL which can be caused by, among others, transition radiation, diffraction radiation, or plasmon decay²².

The amount of CL intensity that is generated by a primary electron depends on the coupling strength which is determined by the overlap between the evanescent field of the fast moving electron and the combined modes of the sample. Unlike for incoherent CL, coherent CL can thus generate a signal when focussed close to a nanostructure^{37,38}. This means that the resolution with which a mode can be imaged not only depends on its brightness but also on the coupling strength. In this chapter, we describe a technique that decouples the resolution and the coupling strength and determines the resolution independent of the imaged mode. To this end, we built a CL model that disentangles the physical structure from the coupling strength. This model is then compared to an SE model which also determines the spatial dimensions of the same structure. By comparing the outcome of both models and applying statistical methods to this, we calculate the accuracy and the precision of the measurements.

This method works best if the physical structure is very well defined, we, therefore, used the edges of almost atomically flat silver nanocubes to determine the resolution. These nanocubes were dropcasted on a 15 nm Si_3N_4 membrane, a high-resolution image can be found in section 2.2.1. It has been shown that such cubes contain multiple surface plasmon resonances³⁹⁻⁴¹. Figure 1 a-d shows the SE contrast and a CL study of one of the cubes. To localize the edge, we made rectangular scans along the cubes and simultaneously recorded the CL intensity, using a photon multiplier tube sensitive in the 230 - 920 nm range, and took an SE contrast at every pixel. See section 2.2 for more information about the system and sample. An example rectangular scan, taken with an electron beam of 30 keV, is shown in Figure 1 f (SE) and e (CL).

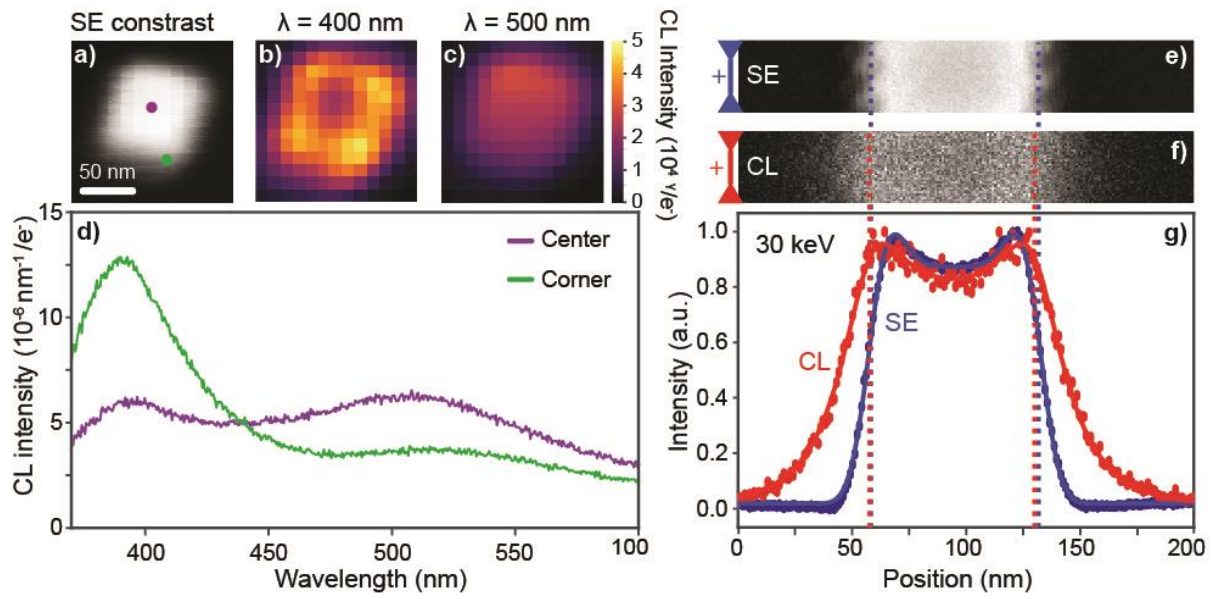


Figure 1 SEM and CL maps and spectra of the atomically flat Ag cubes (a) SE contrast of one of the cubes from which spectra, visible in (d) which were taken at the centre and corner of the cube. In the spectra, two different modes are visible which correspond to a corner mode (b) and a centre mode (c). When a rectangular scan is made along a (different) cube at 30 keV, an SE contrast (e) and CL PMT map (f) are recorded simultaneously. These maps are then summed orthogonal to the scan direction (dots in g) and then fitted with the models explained below (line in g). Both fits find an edge (dashed line in g) from which the resolution can be determined.

To improve the signal/noise ratio, these rectangular scans were summed orthogonal to the scan direction which yields a 1D profile, dots in Figure 1 g. These 1D profiles are fitted with the SE and CL models, explained below (blue/red solid lines in g). From these fits, we determine the CL resolution by comparing where the SE/CL model finds the edge, dashed vertical lines in Figure 1 g. To gain the insight into the phenomena that determine the measured intensities, we first performed multiple simulations.

The SE signal was simulated using CASINO V3.3⁴², a program based on the Monte Carlo algorithm that simulates the electron trajectories in solids. Figure 2 a and c show the side view of a 70 nm Ag cube. The dots indicate where the SE are generated when an electron beam is centred at the top facet. Because the nanocube is smaller than the region of interaction, only the top part is present. This part is more collimated for higher energies which means that for a 30keV beam the area in which SE are generated is more localised than for a 10 keV beam⁴³. If an SE is generated close to an edge, it has a higher chance to escape by that facet, while the escape probabilities through the other sides (top, front, back) are unaffected, yielding a higher overall escape probability. As a result, the SE coefficient, defined as the number of SE that escape from the cube per incoming PE, is higher close to the edge. The dots in Figure 2 b and d show simulated linescans for 10 and 30 keV electron beams with a beam width of 2 or 12 nm (FWHM)⁴⁴. The simulated linescans have a similar shape to the measurement of Figure 1 g and also display the expected peaks close to the edge.

Based on these insights we describe the SE signal generated by a single incoming electron after interaction with a silver nanocube on point x by the integral over the cube of all SE produced inside the cube (C_{SE}), times the probability that this SE is detected, P_{det} :

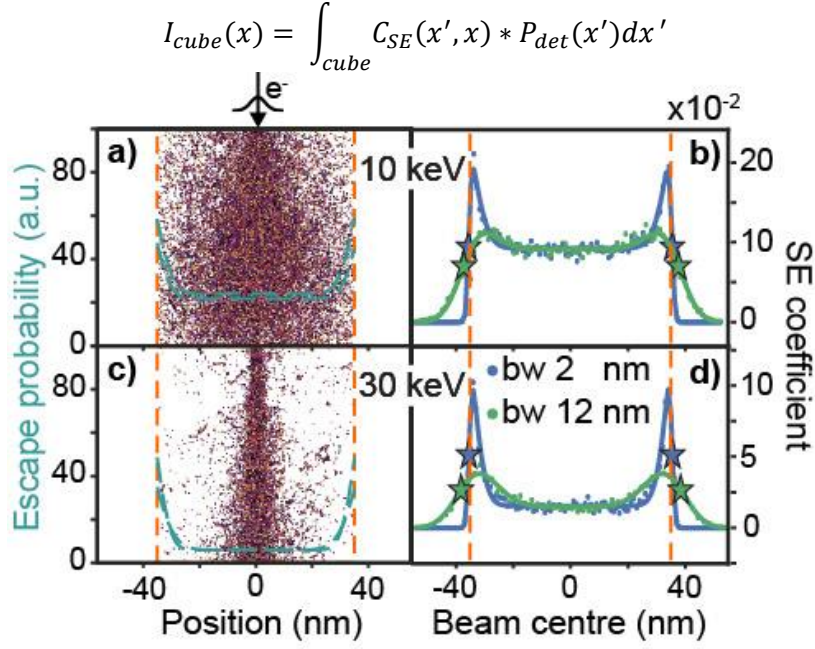


Figure 2 Casino simulations of the electron beam. (a) and (c) Casino simulations of where SE are generated in a 70 nm Ag cube when the electron beam is focused in the centre of the top facet. (b) and (d) SE coefficient of a simulated linescan, with two different beam widths, over an Ag nanocube(dots) fitted with the SE model (line). The orange stripes show the edges and the stars represent where the models estimate them to be. The striped blue lines (a and c) show the escape probability of an SE generated at any depth as calculated by the SE model.

Where $C_{SE}(x')$ is the expected number of SE produced at x' when a PE impacts the sample at x and $P_{det}(x')$ is the detection chance of a SE produced at x' . This model assumes a single electron without a background, for a more realistic description we consider a Gaussian electron beam cantered at c_b , and integrate equation (1) over the electron spread:

$$I_{SE}(c_b) = N_c \int_{spread} I_{cube}(x) * \exp\left(-\left(\frac{x - c_b}{\sigma_u}\right)^2\right) dx + I_{noise}$$

Where N_c is a normalisation parameter and I_{noise} is the sum of all background channels. σ_u is the standard deviation of the total electron spread which is a combination of the beam shape and the vibrations. It is important to stress here that this model does not distinguish between the beam width and the mechanical vibrations of the sample, but rather adds them in the total electron spread. The actual beam width will thus be smaller than what the model finds. A more detailed description of all parameters and the eight fitting variables can be found in section 2.3. To test this model we fitted, it to the simulated data of Figure 2 b and d. The solid line is the fit and the stars are where the model finds the edge. For a beam with a FWHM of 12 nm, the model finds the edge with an error of ~3 nm, therefore the model has a resolution is better than the beam width. The teal dashed line in Figure 2 a and c depict the escape probability that the model finds. The escape probability is in arbitrary units because the model does not distinguish between the number of SE generated and their escape probability. Therefore, the absolute value of the escape probability is less meaningful than its relative change which increases close to the edge for both beam energies, as expected.

The CL simulations were made using MNPBEM17^{45,46}. MNPBEM17 is a Matlab toolbox that uses a BEM approach for solving the Maxwell equations in and outside metallic nanoparticles⁴⁷, and that can also

calculate the CL radiation. That is, it uses the Greens function to calculate the surface charges and currents and derives the CL radiation from that. Because the absolute value of the CL intensity showed discontinuities near the interfaces, we simulated linescans from 1.5 nm up to 140 nm away from the centre of the side facet. The dots in Figure 3 shows such linescans for energies between 10 and 30 keV. The dots are fitted with an exponential decay which thus captures the coupling strength. The simulated cube with a schematic line scan trajectory is displayed in the inset. Just as the SE intensity, the CL signal shows high intensities close to the edge, see Figure 1 f. This could be because the PE couples to modes on the side facet or because the top facet mode is stronger close to the edge than in the centre. This phenomenon can be modelled by assuming two different modes, one uniformly on the top facet and one localized on each side. This yields the following CL intensity for a PE impacting at position x :

$$I_{modes}(x) = N_s \left(\exp \frac{-|x - e_l|}{L} + \exp \frac{-|x - e_r|}{L} \right) + \exp \frac{-|d|}{L}$$

Here the first two exponents correspond to the coupling strength to the two side facet modes, and the third exponent is for the coupling strength to the top facet mode. N_s accounts for the relative strength of the side modes, e_l and e_r are the locations of the left and right edge respectively, L is the

decay length of the coupling strength and d is the distance to the top facet mode which is zero on the cube and the distance to the nearest edge when away from the cube. Just as with the SE model, this has to be integrated over the beam profile and vibrations to yield the total intensity for an electron beam centred at c_b . See the SE model outlined above for how this is done. All parameters, as well as the 7 fitting variables, are explained in more detail in the section 2.4.

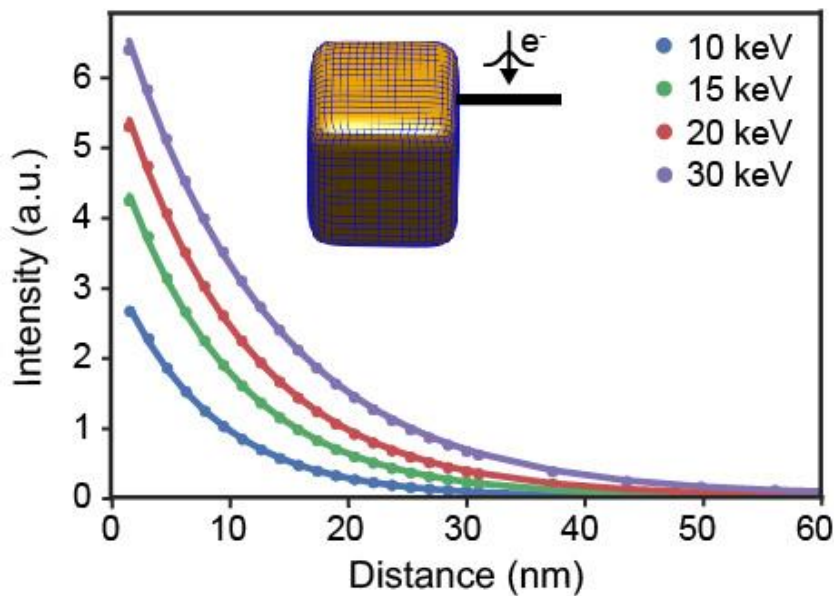


Figure 3 MNPBEM17 simulation of a 70 nm Ag cube (inset) and trajectory (black) along which the electron beam scans. For different energies, the CL intensity is calculated as a function of distance from the cube facet (dots). These simulated data points are fitted with exponentials (lines) yielding the theoretical decay lengths for a silver cube without a substrate.

To determine the resolution, it is important to distinguish between the accuracy and precision. The accuracy is the difference between the average measured value and reality, while the precision is the

consistency between multiple measurements. However, by building up statistics over multiple measurements, it is possible to filter the influence of precision out. That is, by correctly handling the

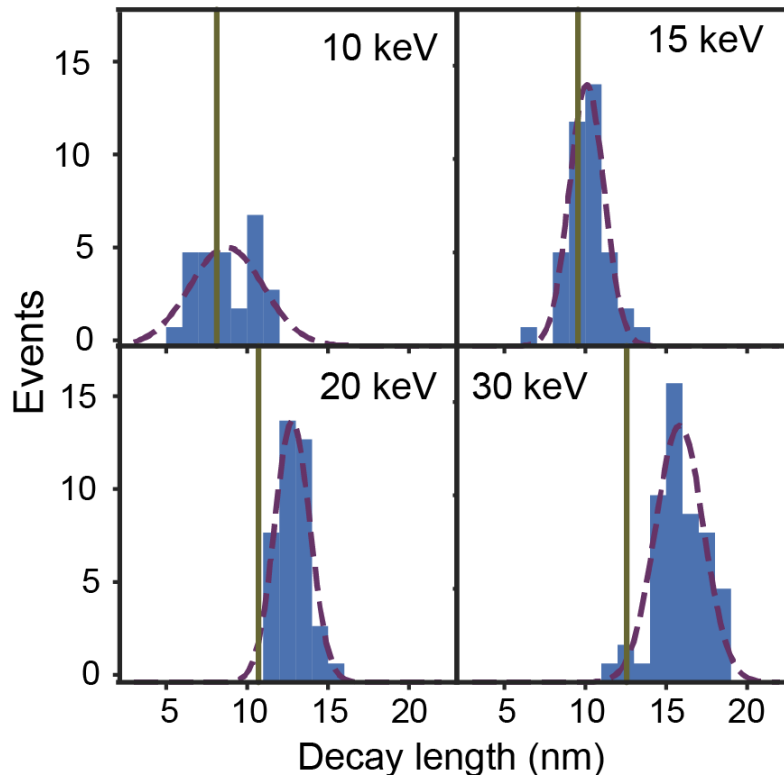


Figure 4 Histograms of the different decay lengths found when fitting the CL model to the Ag nanocubes. The green lines show the decay length found in the simulations of Figure 3. The purple dashed line denotes a Gaussian fit. Note that, since the decay length is assumed the same for all modes, there is one value per scan.

statistics, the resolution only depends on the accuracy. So to determine the full resolution of coherent CL we need to calculate both, which only can be done if there are enough measurements to do statistics. To this end, these models were applied to 159 linescans across different silver nanocubes at 30, 20, 15, and 10 keV of which Figure 1 g and Figure 5 are example scans taken at 30 and 10 keV respectively.

These 159 linescans were selected from 541 scans. The other scans were unusable because they were contamination by carbon. Carbon was problematic because it had a strong influence on both the SE and CL intensity and made it meaningless to apply the models. To consistently filter the contaminated measurements out, we developed multiple tests which are outlined in section 2.5. The histograms in Figure 4 show the fitted decay lengths for four different beam energies. The purple dashed lines indicate a Gaussian that was fitted to the histogram bins and the green line is the value found in the simulations of Figure 3. The centre of the Gaussian is at a higher decay length than the simulated value for all beam energies. This offset increases with beam energy. This could be because the model assumes that the decay length is the same for all modes. This effect would then be more pronounced at higher electron energies because their evanescent field extends further. Alternatively, the presence of a substrate, ligand, or minor carbon contamination, which were not included in the simulations, could influence the decay length of the modes⁴⁸.

The accuracy and precision of these measurements can then be determined by comparing the difference between where the two models fit the edge, ΔL . The left panel of Figure 5 shows a clean measurement done at 10 keV where ΔL is also indicated. ΔL is defined to be positive if the fitted SE edge lays further away from the cube centre than the fitted CL edge. The right panel of Figure 5 shows a histogram of this difference for four different beam energies. The position of the Gaussians that are fitted through the bins gives the accuracy while the width denotes the precision. The widths of the Gaussians range from 4.2 to 7.4 nm. This indicates that a sub 5 nm precision is possible. The centre of the Gaussians changes from -3 nm to 1.5 nm when the beam energy changes from 10 to 30 keV. This variation seems to imply that the model neglects some effects that depend on the beam energy, which is discussed in more detail in sections 2.3 and 2.4 for the SE and CL model respectively. As a result, the accuracy of our measurements has a small energy dependence. Nevertheless, the average accuracy is ~ 2 nm which is significantly lower than the precision.

In conclusion, we built two models that predict the SE and CL signal from an electron beam centred on or close to a silver nanocube. These models were used to find the 318 edges of 159 measurements. Doing statistics on the difference between where these two models found the edge allowed us to decouple the accuracy and precision. Hereby it is possible to determine the resolution of coherent CL independently of the imaged mode. On our setup, this procedure yielded an accuracy of 2 nm and precision of less than 5 nm. This is significantly less than the combination of vibration and beam width which is around 17 nm, see section 2.2.3. This method could be used in any CL setup to determine the resolution and is readily adaptable for EELS spectroscopy.

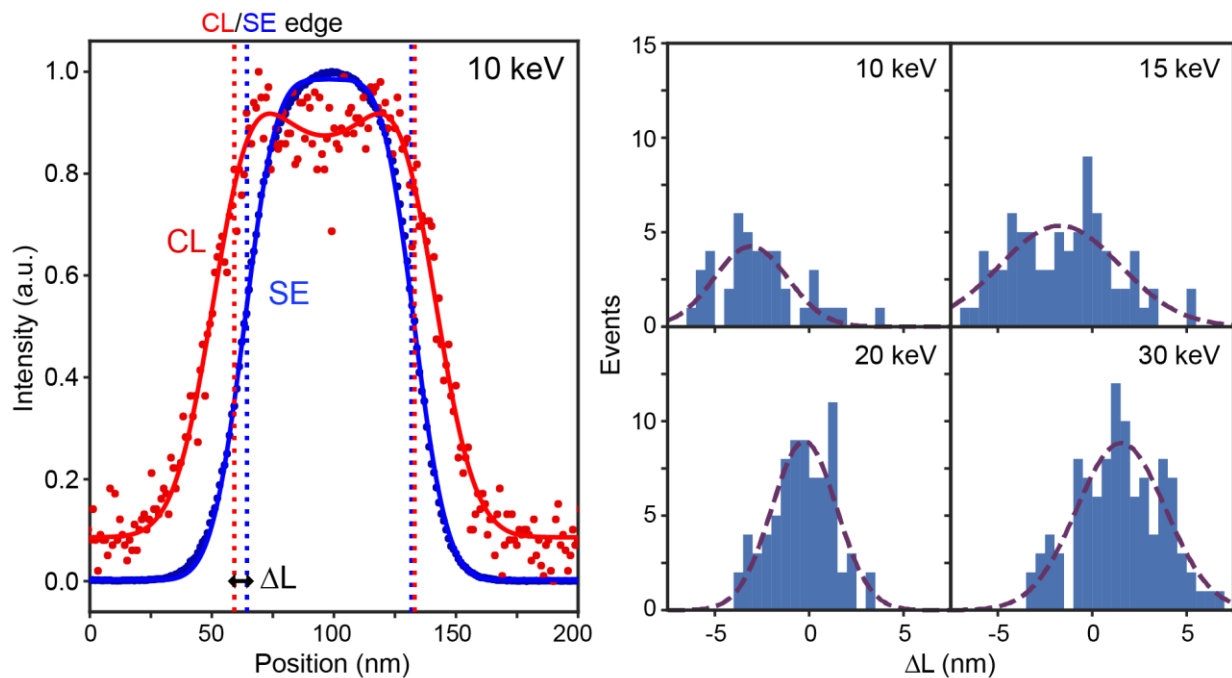


Figure 5 Application of the SE and CL model to the data to determine the resolution. **left)** CL and SE intensity at 10 keV and fit (dots and lines respectively). Stripes indicate CL and SE edges according to the fits. **Right)** histograms of ΔL , the difference between these two values at different energies. ΔL is defined as being positive if where the model fits the edge for SE is further from the centre than for CL. The purple dashed lines are Gaussian fits through the centres of the bins. Note that there is one value per edge and thus two values per scan.

2.2 SYSTEM AND SAMPLE

A schematic drawing of the system in which all cathodoluminescence measurements were done can be found in Figure 6 as well as a picture of the system. The microscope is a Quanta 650 FEG SEM from Thermo Fisher/FEI equipped with a Delmic CL system (SPARC). The CL intensities are taken with a Photon Multiplier Tube from Hamamatsu, the H10721-20, that detects all photons between 230 and 920 nm. Using this setup the electron beam is rastered over the sample, and an SE contrast and either a spectrum or the PMT intensity is taken at every pixel.

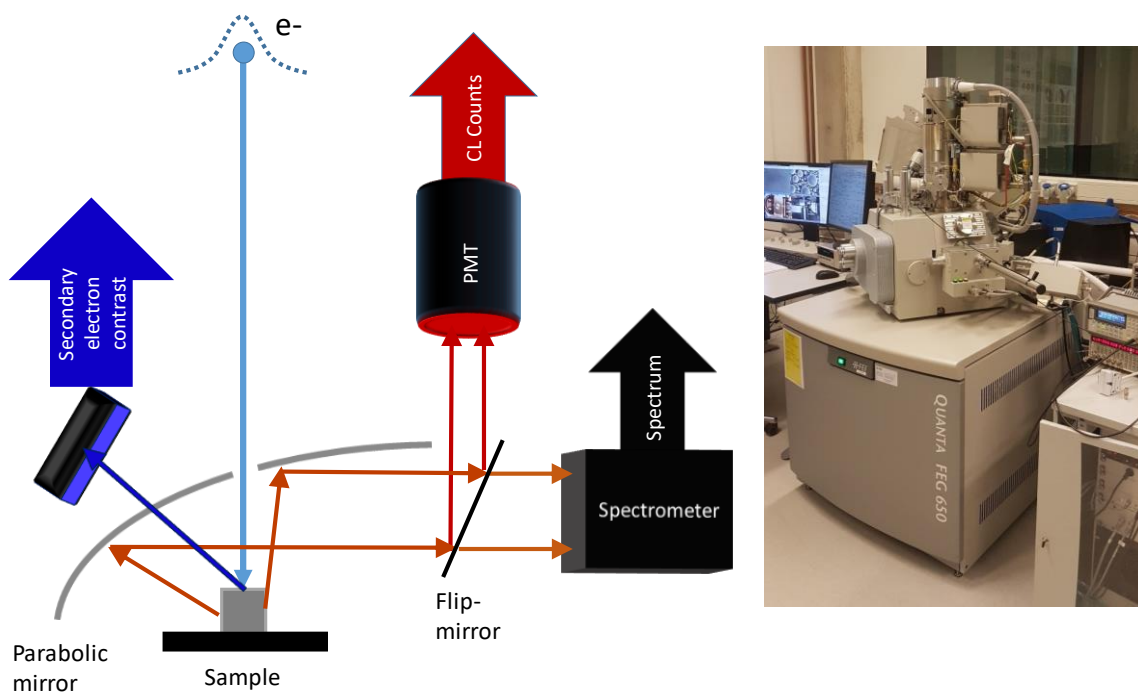


Figure 6 Experimental setup. **Left**, schematic in which the electron (light blue) travels through a hole in the parabolic mirror to the sample. The sample then emits light (orange) and secondary electrons (dark blue). The light can be either send to a spectrometer or, by way of a flip mirror, to the photon multiplier tube (PMT). The electron beam is then rastered over the sample and a SE intensity and either a spectrum or CL contrast are taken at every pixel. **Right**, picture of the setup, the spectrometer and the PMT are located in the black and blue box attached to the back of the column. N.B. In the microscope the actual position of the SE detector is right of the parabolic mirror, close to where the spectrometer is on this schematic.

2.2.1 Sample preparation

The cubes were chemically grown by Harshal Agrawal at AMOLF and drop-casted on a TEM grid. The cubes were single crystalline⁴⁹ and have size dispersion of 75 ± 5 nm. Originally the cubes contained Polyvinylpyrrolidone ligands but, since they increased carbon contamination, were later chemically removed. A HAADF-STEM image of one of the cubes, taken on a Verios G4 XHR from thermosFisher, can be seen in Figure 7.

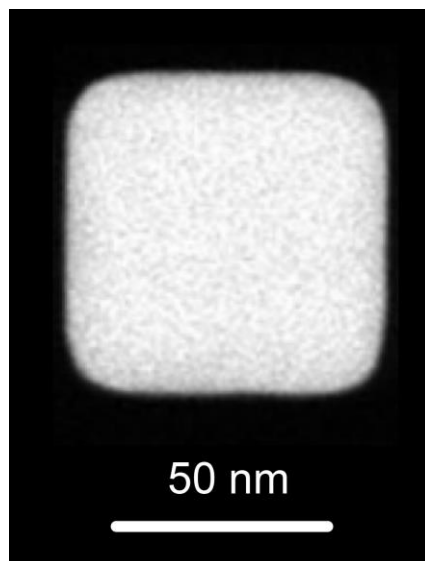


Figure 7 HAADF-STEM image of one of the Ag nanocubes used in this paper, taken by Harshal Agrawal.

2.2.2 Cube width

Using the models described in the main text, the widths of the cubes can be calculated. The resulting width distributions are a combination of the precision of the measurements and the intrinsic spread in cube size. Figure 8 shows a histogram of the found values with a Gaussian fitted through the centres of the bins. The centres of both fits are at 69 nm, which is on the lower end of the expected size dispersion. The excellent agreement between the two models supports the finding of the main text, that repeated measurements can drastically improve the resolution with which spatial objects can be resolved. For the individual measurements of the cubes, the calculated widths differ significantly between the SE and CL models. However, these differences factor out when averaged over multiple measurements. From these fit, we also see that the precision of an SE measurement is better than for CL. This difference is visible by the fact that the FWHM of the SE Gaussian fit is 14 nm while that of the CL fit is 16 nm.

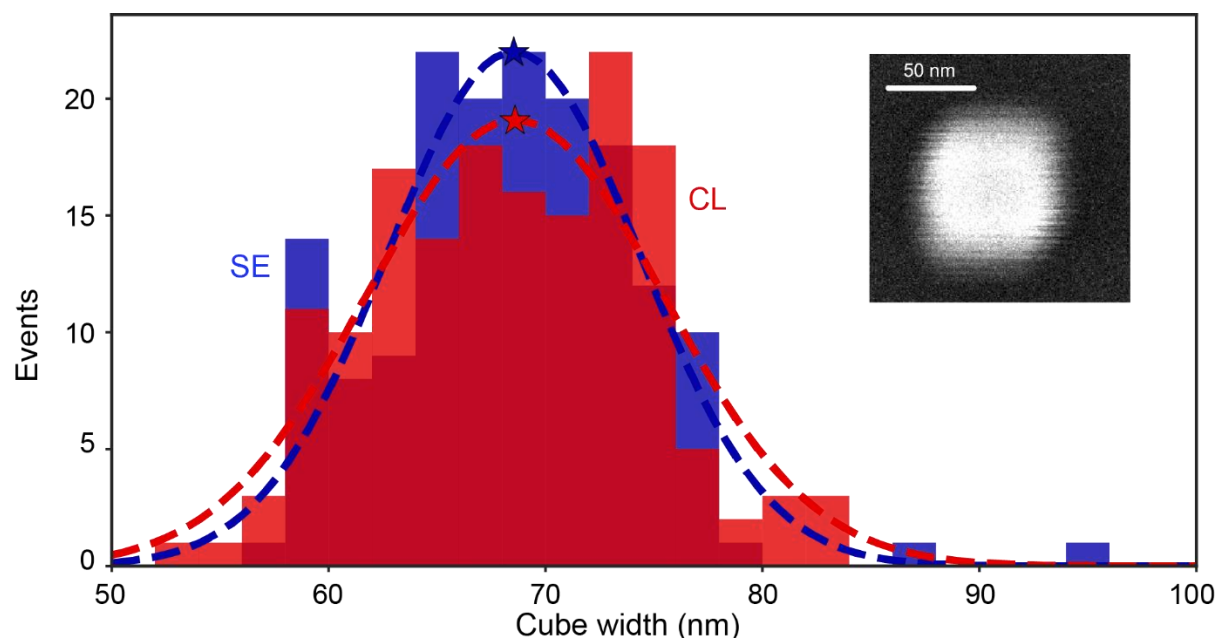


Figure 8 Histogram of the width of the cubes as calculated by the SE and CL models with Gaussian functions fitted through them. The stars indicate the tops of the Gaussians. An example SE image with strong vibrations is shown in the Inset

2.2.3 Beam diameter

The beam diameter is an important system parameter which was included in both models as part of the total position uncertainty, see sections 2.3 and 2.4. This means that it is possible to use the models to help characterize the system. The position uncertainty as fitted by the models is a combination of the beam diameter and the mechanical vibrations. In our experiment, there were two sources of mechanical vibrations, those inherent to the system and those caused by the construction of a new building next to the experimental hall. The influence of this construction pit can be seen in Figure 9, which shows a scatter plot of the total uncertainty as found by the SE model vs the CL model. Two clusters of measurements are visible, one with high total uncertainty and one where it was significantly less. When looking at the days on which these measurements are taking we see that the amount of vibration depended a lot on the day, something we also observed during measurements. We, therefore, believe that the difference between the two clusters is whether or not the construction site was using heavy machinery. When quadratically subtracting the centres of the two different area's we find that the construction site on its own would cause vibrations of approximately 20 nm, see inset in Figure 8 for an example. Another noteworthy feature of Figure 9 is that there is a robust correlation between the uncertainty found by the two models. The closer a marker is to the grey dashed line the better the agreement on the total uncertainty by the two models.

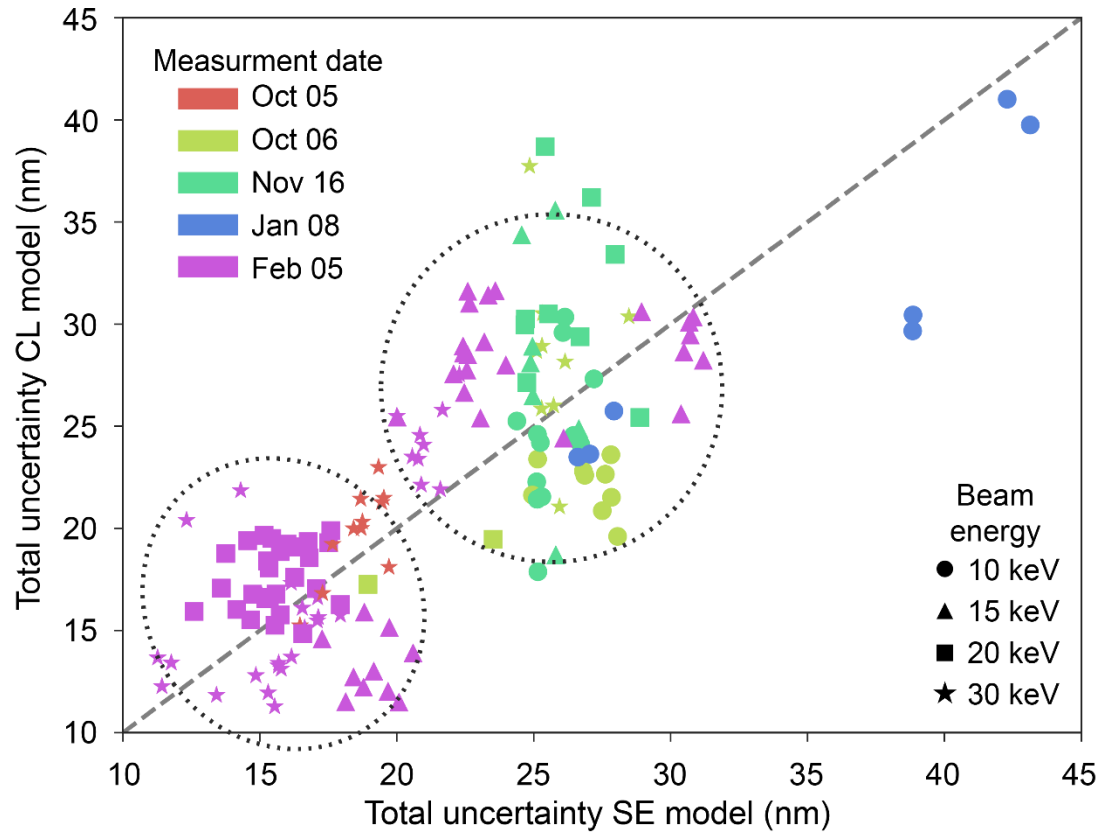


Figure 9 Beam width (FWHM) as found by the different models. The markers indicate the beam energy used during the measurement and the colour depends on the day the measurement was taken. On the grey diagonal dashed line, the uncertainty as found by SE and CL model is the same. Thus, the closer a fit is to the dashed line the better the agreement between the two different models. The dotted circles are drawn around the two clusters of measurements. The difference between them seems to come from vibrations caused by heavy machinery in a neighbouring construction site.

2.3 THE SE MODEL

2.3.1 Concept

Before we can construct a model that describes the SE signal it is useful to consider all phenomena that contribute to the signal. The microscope used produces an electron beam with a spread around the centre which induces an uncertainty into where on the cube the electron will hit. This uncertainty is increased by the mechanical vibrations of the cube. Furthermore, the secondary electrons (SE) are generated in a pear-shaped region, of which the exact form depends on the sample properties, below the impact point. Finally, we have to consider the fact that, to be detected, an electron has to escape the sample. This chance depends on where the SE are generated, as will be outlined in more detail below. All this is schematically shown in Figure 10 and is the basis on which we build a model for the total SE signal of an electron beam centred on point c_b .

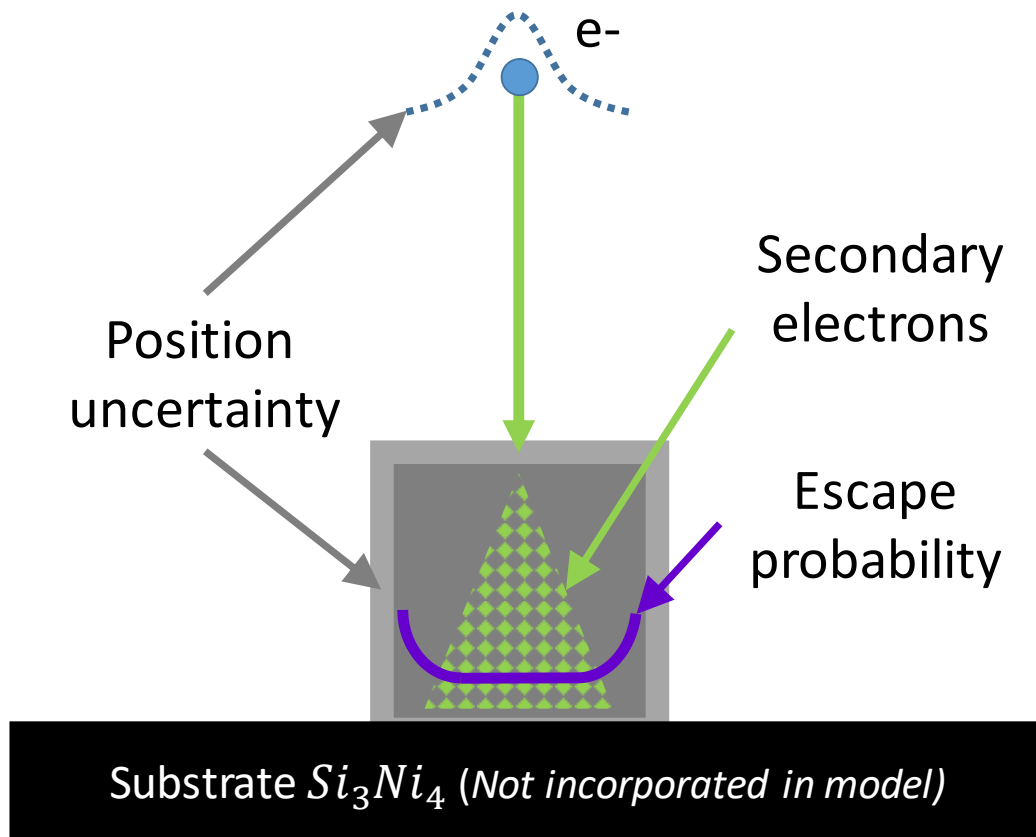


Figure 10 schematic representation of the SE model. An electron hits a silver nanocube on the top and generates multiple secondary electrons. These secondary electrons have a certain chance to escape which is higher towards the edge. Both the cube and the primary electron have an uncertainty in their position, the electron due to the beam spread and the cube due to mechanical vibrations.

2.3.2 Mathematical model

The model contains two different uncertainties in the position of the e^- , one caused by the beam spread and one from the mechanical vibrations of the sample. Because both depend on a complex interplay of

multiple variables, we apply the central limit theorem and assume both to be Gaussians. The beam spread is then given by $\exp\left(-\left(\frac{x-c_b}{\sigma_b}\right)^2\right)$ where σ_b is the beam spread, x the position where the electron hits the cube and c_b the beam centre. The uncertainty caused by the sample vibrations is modelled with $\exp\left(-\left(\frac{x-x'}{\sigma_v}\right)^2\right)$ where σ_v is the vibration spread, x is where the sample is displaced to and x' is where it would be without displacement. In the model, these two uncertainties are captured in one variable, which is possible because there is no difference between the sample being displaced a distance d or the electron being displaced $-d$. This assumes that the cube undergoes multiple vibrational cycles per measurements. Since the vibrations had a frequency of $\sim 300\text{Hz}$ and measurement times per pixel were in excess of 200 ms, this is justified. These two uncertainties can then be added together to yield a total positional uncertainty that is given by $\exp\left(-\left(\frac{x-c_b}{\sigma_u}\right)^2\right)$, where σ_u is the total uncertainty on the measurements which is given by $\sigma_u^2 = \sigma_b^2 + \sigma_v^2$. From this we can calculate the total SE intensity as a function of c_b by integrating over each point where an electron can hit the sample, multiplied by the signal of a single electron that hits the cube at that point:

$$I_{SE}(c_b) = N_{SE} \int_{spread} I_{cube}(x) * \exp\left(-\frac{(x-c_b)^2}{\sigma_u^2}\right) dx + I_{noise}$$

Where N_{SE} is a normalisation parameter and I_{noise} is the average of all the background channels including from the substrate and detector noise. $I_{cube}(x)$ is the SE signal from an electron that hits the sample at point x . This is given by the integral over all the SE that are produced multiplied by their respective escape probability.

$$I_{cube}(x) = \int_{cube} C_{SE}(x', x) * P_{detection}(x') dx'$$

Here $C_{SE}(x', x)$ is the number of SE generated at point x' if the PE hits at point x , and $P_{detection}(x')$, the chance an SE produced at x' is detected. To simplify the problem, we assume that all SE are produced at the same height. Furthermore, we assume that the relative number of SE produced is given by a normal distribution inside the cube and is 0 outside the cube:

$$C_{SE}(x', x) = \begin{cases} N_p * \exp\left(-\frac{(x' - x)^2}{\sigma_p^2}\right) & | e_l < x < e_r \text{ and } e_l < x' < e_r \\ 0 & | \text{ else} \end{cases}$$

Here N_p is the total number of SE produced, in the fitting this has been incorporated in N_c . σ_p is the spread of the SE production, and e_l and e_r are the left and right edges of the cube respectively. For a SE to be detected, it needs to escape either through the top facet or through one of the side facets. The escape probability out of the top facet is independent of the x -position while the escape probability towards the sides is location dependent. The chance a SE escape through a side facet depends on the complex interplay of, among other things, the initial direction of the SE, the height at which the SE is generated, and the SE energy. Here we approximate it by assuming that these parameters together must be above a certain threshold that decreases close to the edge. If the interplay of variables is normally

distributed the fraction of SE that is expected to surpass the threshold is given by a cumulative normal distribution function (CDF). This yields the following formulas for the chance a particle is detected, $P_{detection}$, based on the contributions from the sides, P_{sides} , and the top, P_{top} .

$$P_{detection}(x') = (P_{sides}(x') + (1 - P_{sides}(x')) * P_{top})$$

$$P_{sides}(x') = N_{detection} \left[\text{CDF} \left(\frac{x' - e_l}{\sigma_{detect}} \right) + \left(1 - \text{CDF} \left(\frac{x' - e_r}{\sigma_{detect}} \right) \right) \right]$$

Here P_{top} is a constant and $N_{detection}$ is a normalisation parameter that is incorporated in N_{SE} in the fitting, in this case, it also captures the height of the aforementioned threshold. σ_{detect} can be seen as the region in which escape through the sides contributes significantly to the total escape probability.

2.3.3 Implementation

In total the model has eight fitting parameters that account for; normalisation, left edge, right edge, background, combined uncertainty, relative escape probability through the top facet, and region in which escape through the side is significant. Figure 11 Examples of how different parameters change the shape of the SE model. σ_u is the total uncertainty, P_{top} is the relative change an SE escapes through the top facet, σ_{detect} is the region in which the side facets contributes significantly to the escape probability and σ_p is the width of the Gaussian in which the SE are produced. Per subplot one parameter is changed while the other are kept constant. These values are 0.2 for P_{top} and 10 for σ_{detect} , σ_u and σ_p . shows how the last four parameters influence the shape of the SE signal. Increasing the total position uncertainty, σ_u , makes the whole signal more spread out and smoothens out any features. Nevertheless, the centre of the signal remains at the same place. In the graph, all four lines seem to cross at the same point but when zooming in it is clear that this is not the case. When the relative chance to escape through the top, P_{top} , increases, the total signal goes up, and the contribution from the sides goes down. This is because if an electron already escapes through the top facet, it can no longer leave through the side. Expanding the region in which the escape through the sides is relevant, σ_{detect} , increases the signal of the cube and makes the peaks more prominent. The latter might be counter-intuitive but is readily explained by realising the following. If a focused electron beam is centred next to the edge, a significant number of electrons are generated in the centre of the cube. If σ_{detect} would be very small, the number of electrons that escape through the side would thus be minimal as well, making the peaks unnoticeable. If σ_{detect} is increased to the point where escaping through the side has the same likelihood throughout the cube the peaks disappear again. The point where this happens is strongly correlated with the spread of the SE production in the cube, σ_p . The more localised the SE production, which in our experiment corresponds to a higher beam energy, the more prominent the peaks.

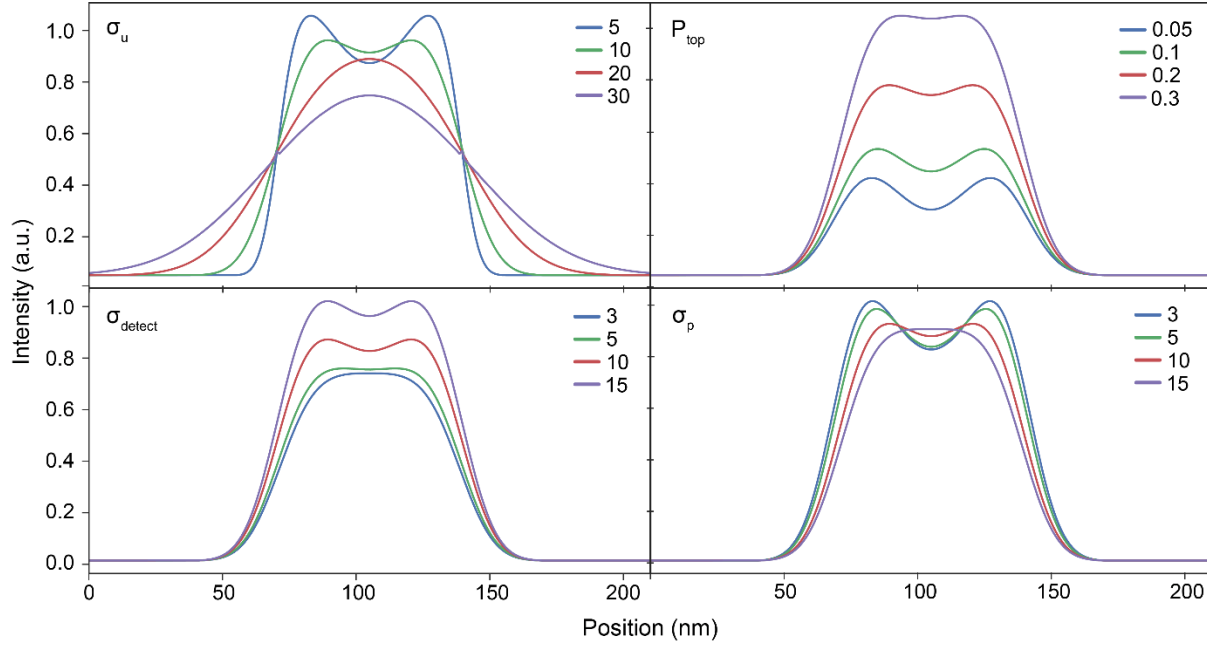


Figure 11 Examples of how different parameters change the shape of the SE model. σ_u is the total uncertainty, P_{top} is the relative change an SE escapes through the top facet, σ_{detect} is the region in which the side facets contributes significantly to the escape probability and σ_p is the width of the Gaussian in which the SE are produced. Per subplot one parameter is changed while the other are kept constant. These values are 0.2 for P_{top} and 10 for σ_{detect} , σ_u and σ_p .

2.4 THE CL MODEL

2.4.1 Concept

Just as with the SE model, it is essential to know which phenomena influence the CL signal when building a model. Besides the position uncertainties caused by the beam spread and the mechanical vibrations, which we already analysed in the SE model, we now need to consider the evanescent field of the fast-moving electron and the mode profile of the surface plasmon. This is because the overlap between these two field distributions determines the likelihood of excitation, the coupling strength.

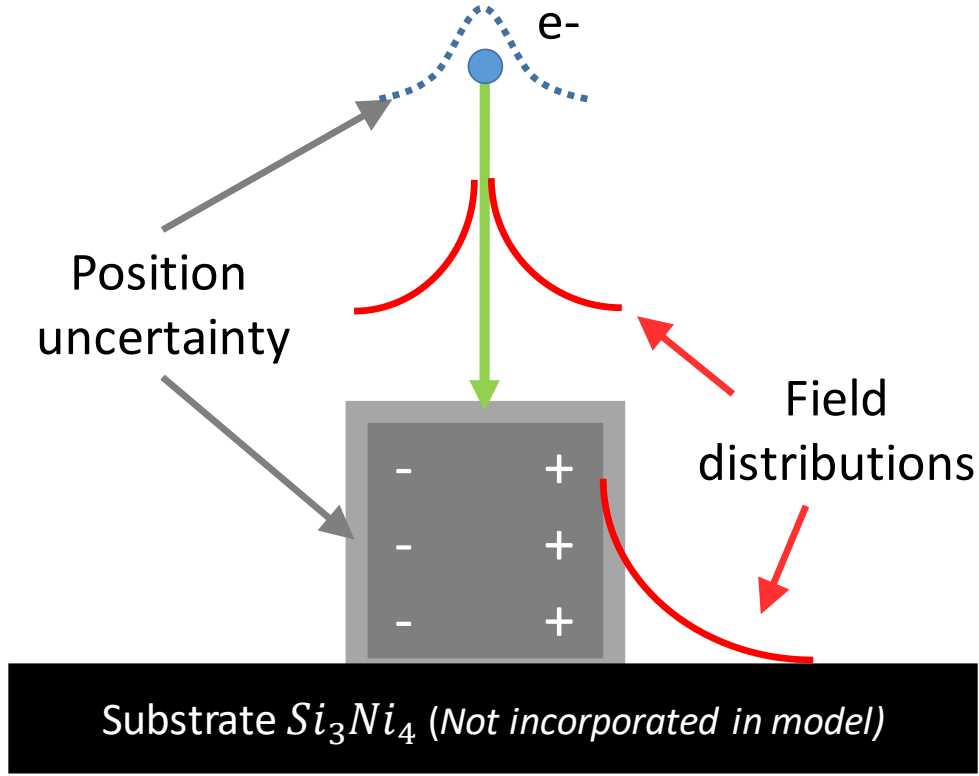


Figure 12 Schematic representation of the CL model. An electron couples to a surface plasmon mode inside a silver nanocube. The coupling strength of this interaction is determined by the overlap of the field distributions of the mode and the evanescent field of the fast-moving electron. Both the cube and the electron have an uncertainty in their position, the electron due to the beam spread and the cube due to mechanical vibrations.

2.4.2 Mathematical model

For the reasons outlined in the description of the SE model, we can combine the uncertainties caused by the beam spread and mechanical vibrations in the term $\exp\left(-\left(\frac{x-c_b}{\sigma_u}\right)^2\right)$ where σ_u is the total uncertainty on the measurements which is given by $\sigma_b^2 + \sigma_v^2$. By integrating over the combined uncertainty, multiplied by the amount of signal that is produced at that position, we get the total CL signal:

$$I_{CL}(c_b) = N_{CL} \int_{spread} I_{modes}(x) * \exp\left(-\frac{(x - c_b)^2}{\sigma_u^2}\right) dx + I_{noise}$$

Here N_{CL} is a normalisation parameter, and I_{noise} is the average of all the background signal such as from the substrate and electric noise. $I_{modes}(x)$ is the total CL signal from all bright modes if an electron hits the sample at point x . While the cubes have many more modes⁴¹, some of these do not decay radiatively and are called dark modes³⁶. We found that the minimum number of modes that could describe the data was three, one on each of the two relevant sides and one on the top facet. The resulting CL intensity from a single electron that crosses the surface at x is then given by:

$$I_{modes}(x) = N_s * \left(\exp \frac{-|x - e_l|}{L} + \exp \frac{-|x - e_r|}{L} \right) + \exp \frac{-|d|}{L}$$

Here N_s is the relative strength of the side facet modes compared to the top facet. L is the decay length of the coupling strength, e_l and e_r are the left and right edges of the cube respectively, and d is the distance to the top facet mode. This distance is 0 when the electron hits the top facet and the distance to the nearest edge otherwise:

$$d = \begin{cases} 0 & | e_l < x < e_r \\ \min(|e_l - x|, |e_r - x|) & \text{else} \end{cases}$$

2.4.3 Implementation

The resulting CL model has seven fitting parameters that account for; normalisation, left edge, right edge, background, combined uncertainty, decay length, and relative strength of the side modes. Figure 13 shows how the last three parameters influence the shape of the CL signal. Just as with the SE model, increasing the total position uncertainty, σ_u , smears out all observable features. When decay length of the modes, L , is increased the CL signal falls off more slowly away from the cubes and the peaks on the side of the cube become more pronounced. The latter is related to the positional uncertainty. If a beam is cantered next to the edge, there are still electrons that hit the centre of the cube. If the decay length is very short, a lot of these cubes will not feel the effect of the mode on the side of the cube, resulting in a lower peak. Increasing the decay length to the point where the coupling strength does not significantly decrease on the length scale of the cube removes the peaks again, as expected. The final parameter shown in Figure 13 is the relative strength of the side modes, N_s . If this is increased the peaks become a lot more pronounced.

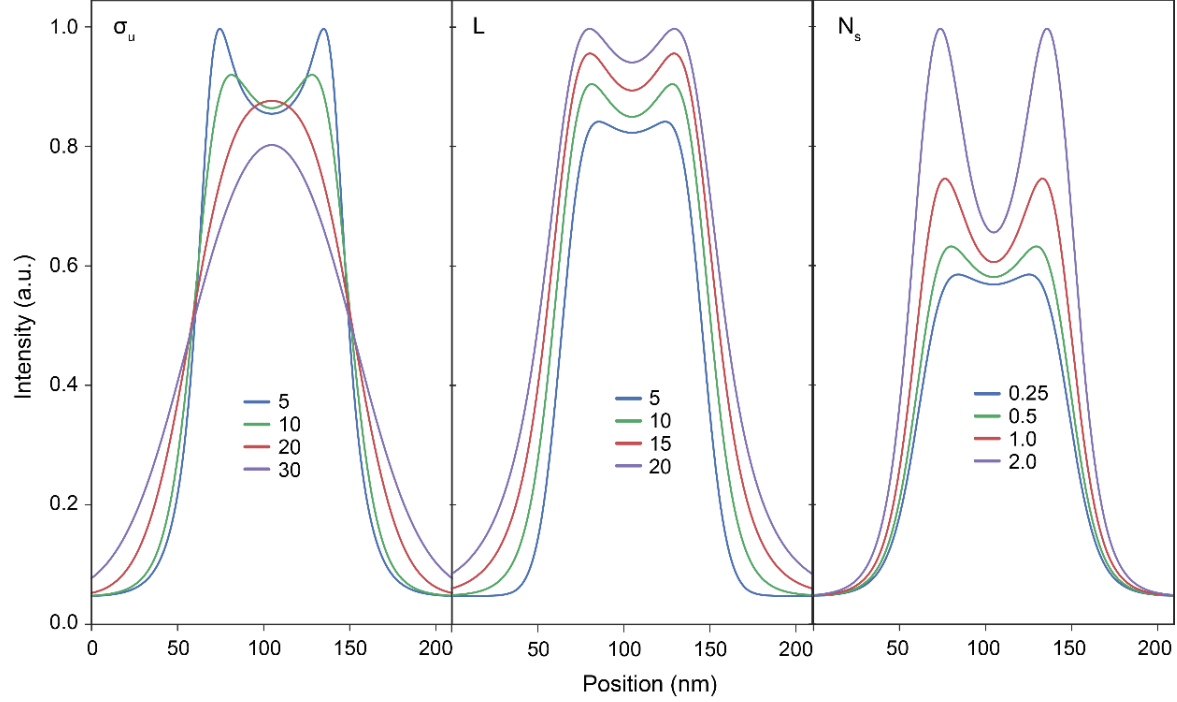


Figure 13 Examples of how different parameters change the shape of the CL model. σ_u is the total uncertainty, L is the decay length, and N_s is the relative strength on the side surface plasmons compare to the top surface plasmon. Per subplot one parameter is changed while the other are kept constant. These values are 10 for σ_u , and L and 0.4 for N_s .

2.4.4 MNPBEM17

In the main text, this model was tested using MNPBEM17, a Matlab toolbox that uses a boundary element method (BEM) to solve the Maxwell equations in the presence of dielectric media. BEM works by calculating boundary charges and currents from which the electromagnetic field can be derived. These, in turn, form the basis from which the EELS and CL signal can be calculated⁴⁷. Besides providing simulations to which the model can be tested, MNPBEM17 can thus also simulate the CL spectrum of the Ag nanocube and plot the mode distribution^{45,46,50}. In Figure 14 the CL spectra for a 10 and 30 keV electron beam, sent to a 70 nm Ag nanocube, are shown. The 30 keV measurement can be compared to the spectrum and CL maps of Figure 1 a-d, which were also at 30 keV. In the experiment a peak is visible at 400 nm, corresponding to a corner mode, and a smaller peak around 500nm, which corresponds to a centre mode. In the simulations only the corner mode is visible, this could be due to a different dielectric constant⁵¹ or because the substrate and ligands around the measured cube break some symmetry. The only simulated mode without a strong presence at the corners was at an energy of 3.7 eV. The distribution of the corner mode observed by the measurement and the first centre mode as calculated by MNPBEM17 are plotted in Figure 15.

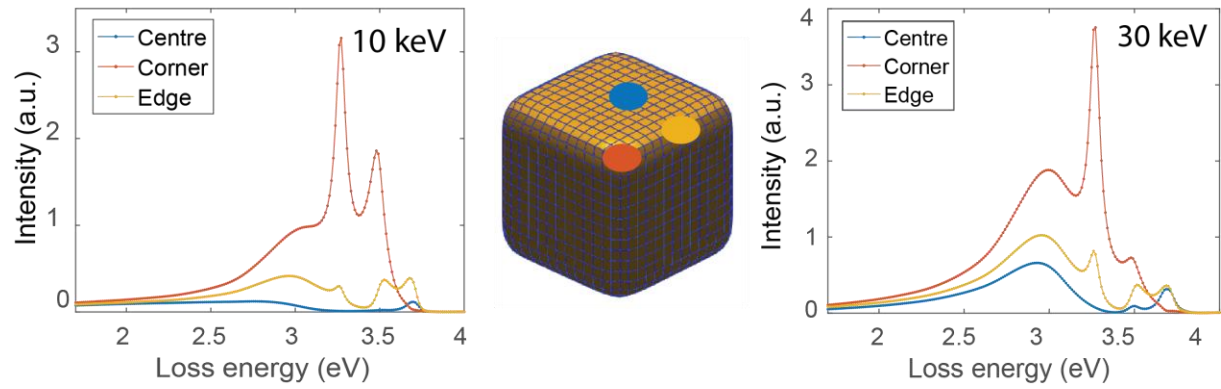


Figure 14 Spectra of Ag nanocube as calculated by MNPBEM17. The spectra are at 10 and 30 keV (left and right respectively) and are taken on the points indicated in the simulated silver nanocube in the centre.

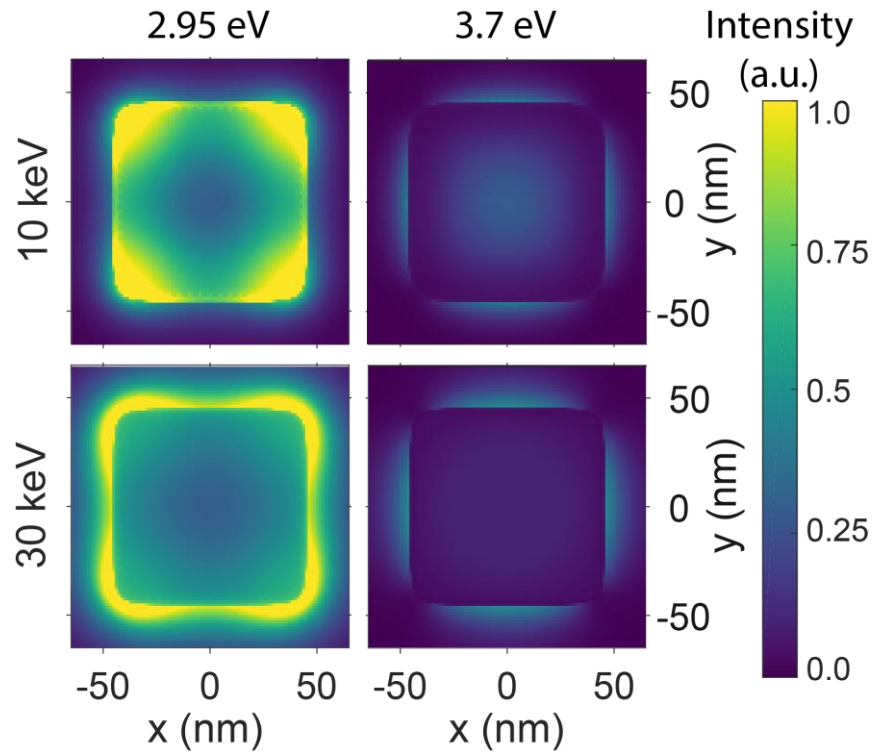


Figure 15 CL intensity as calculated by MNPBEM 17. The light from the higher energy beam comes from a larger region of which a significant portion is outside of the cube. This is because the evanescent field of the electron, and therefore the coupling strength, is more spread out.

2.5 DEALING WITH CARBON CONTAMINATION

2.5.1 Evidence of contamination

Historically, carbon deposition, and its influence on the SE signal has always been a factor in electron microscope experiments⁵². The fast-moving electrons crack hydrocarbon molecules that are present in the vacuum chamber and, possibly, on the sample in the form of dirt or ligands⁵³. The electron beam then attracts these particles which form a layer on and around the measured area. This decreases the contrast of the SE image because it covers up the features and smoothens them out. Carbon also blocks part of the light emitted by nanostructures below it, thereby reducing the CL signal⁵⁴. During most of the measurements a significant carbon ring formed around the cubes, an example of this is visible in Figure 16 a. This had a strong influence on both the SE and CL signal as can be seen when Figure 16 b is compared with the measurements from the main text, Figure 1 g and Figure 5. In later samples, this was partially mediated by removing the ligands around the cubes, but the issue remained. To filter these measurements by hand was undesirable for two reasons. First of all the number of measurements would make it a very time-consuming task. More importantly, however, was that the effects of the carbon deposition were sometimes very subtle and it would be impossible to stay consistent when filtering by eye. We, therefore, developed an automatic procedure that could screen the contaminated measurements.

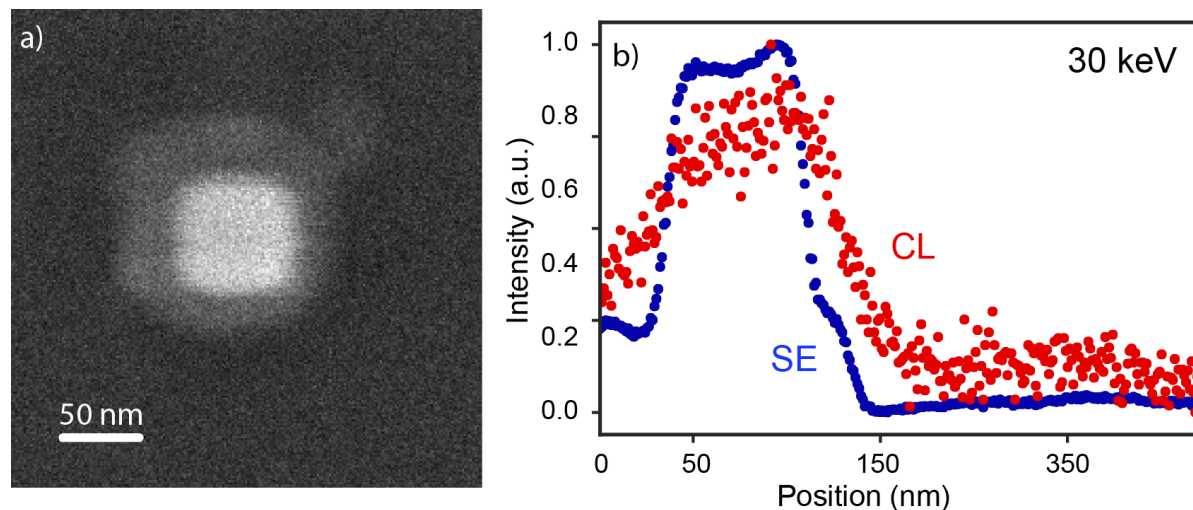


Figure 16 Influence of carbon on measurement. **(a)** Ag nanocube after measurement. The bright core is the cube itself and the light grey area around it is carbon that has been deposited during the measurement. **(b)** SE and CL intensity as measured along the cube in a).

2.5.2 Filtering procedure

The first step in this procedure was to fit a simplified version of the SE model, outlined in section 2.5.4, to the cubes. The reason we used the SE data to determine whether a cube was contaminated is that the signal to noise ratio was a lot higher for SE than CL. A simplified model was used rather than the extensive one because the computational resources needed for the extensive model made it too slow. The

simplified model approximates the double integral which makes it significantly faster, but it strips the fitting parameters from most of their physical meaning. Nevertheless, it is capable of fitting the SE data well enough to distinguish between clean and contaminated measurements. After the simplified SE model was applied to all measurements they had to meet the following criteria to be considered clean:

1. **Orientation**

Only scans that were perfectly perpendicular to, and centered on, the side facet of a single nanocube were used. This criteria mostly filters measurements where the drift correction failed. We also made some scans of multiple adjacent cubes or diagonal over the cubes which we removed in this step. These phenomena were directly visible in the SE map after measurement and were thus not filtered out based on the CL line scan.

2. **Symmetry**

Carbon deposition is often asymmetric, so if either the SE or the CL signal was asymmetric, the measurement was discarded. An example of a cube that was filtered based on this is visible in Figure 17 a. The asymmetry was calculated by summing the difference in signal between the first 70 nm left and right of the centre of the cube. The centre was taken to be in the middle of the two edges as found with the simplified SE model.

3. **Side escape probability to high or low**

As explained in the previous chapter an SE that is generated close to one of the sides has a high chance to escape through it. However, if one of the sides of a cube is contaminated with carbon, the escape probability of the corresponding edge is reduced. This is because the carbon imposes a barrier that lowers the escape probability from that side. Alternatively, the carbon deposition could influence the measurements to such a degree that the model fitted a ridiculously high escape probability through the sides. Therefore, cubes, with either a very high, Figure 17 b, or very low, Figure 17 c, ratio of escape probability through the sides vs that of the top facet, were not considered.

4. **General bad SE fit**

Sometimes the SE model did not fit for different reasons than the ones outlined above. The most common was a small symmetric carbon deposition that was thin enough to let the SE escape through the sides but thick enough to influence the measurements. These measurements were filtered out in this step, see Figure 17 d for an example.

5. **Extensive model**

If all criteria outlined above were met, the complete SE and CL models were applied to the measurement. Out of the 541 linescans made 183 made it until this step. Here we again placed some constraints on how well the extensive models should fit. This caused another 14 measurements to be discarded. An example of a measurement that was rejected here is visible in Figure 17 e.

6. **Plotting**

For some cubes, mostly at 10 keV, the CL and SE signal overlapped very well on one edge but not

at all on the other side. This again is most likely due to one-sided carbon deposition. Alternatively, the cubes could have been oriented in such a way that one side was directly facing the SE detector and the other was facing away from it. An example of this is visible in Figure 17 f. From these cubes, we used the clean edge but disregarded the other one. In the end, this had very little effect on the resolution as we discuss below in section 2.5.3.

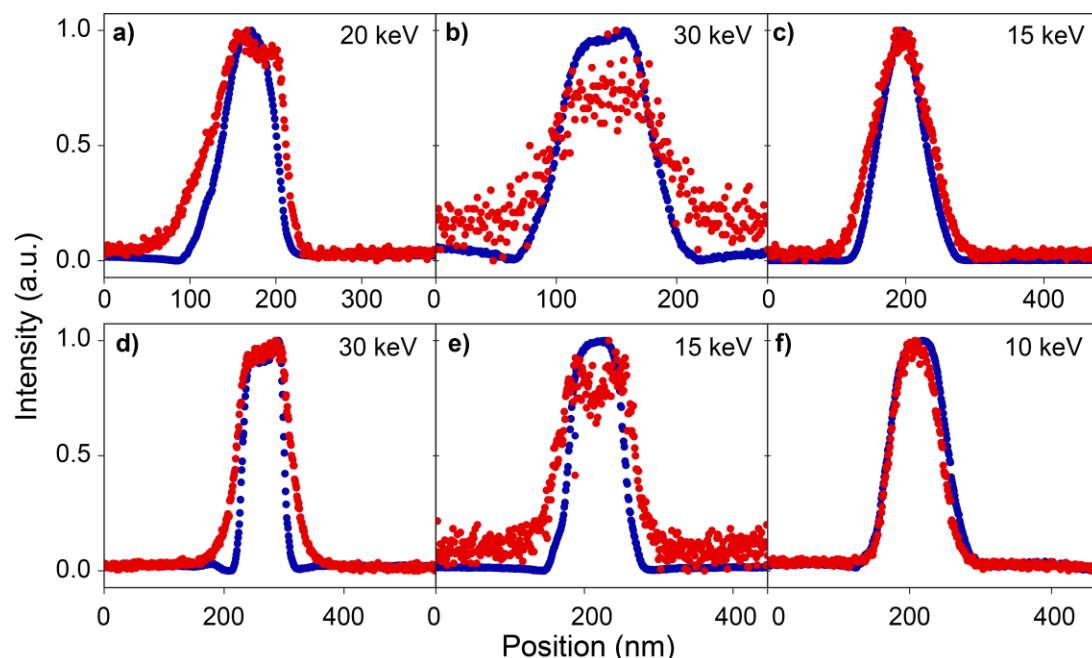


Figure 17 Examples of measurements that were filtered out because they were contaminated with carbon. (a) was too asymmetric, the escape probability through the side was too high for (b) and too low for (c). (d) was rejected because the simplified model didn't fit well enough and (e) because the extensive model didn't fit well enough. For (f) the left edge was considered, but the right edge was not.

2.5.3 Robustness of procedure

The filtering done in step 6 could seem a little arbitrary. To test the robustness of the filtering process, Figure 18 shows the histograms with (left) and without this filtering step (right). The Gaussians that are fitted through the bins are almost unchanged by the filtering, showing that our statistics are robust. The fit values for the Gaussians with and without the screening of step 6 is presented in the table below.

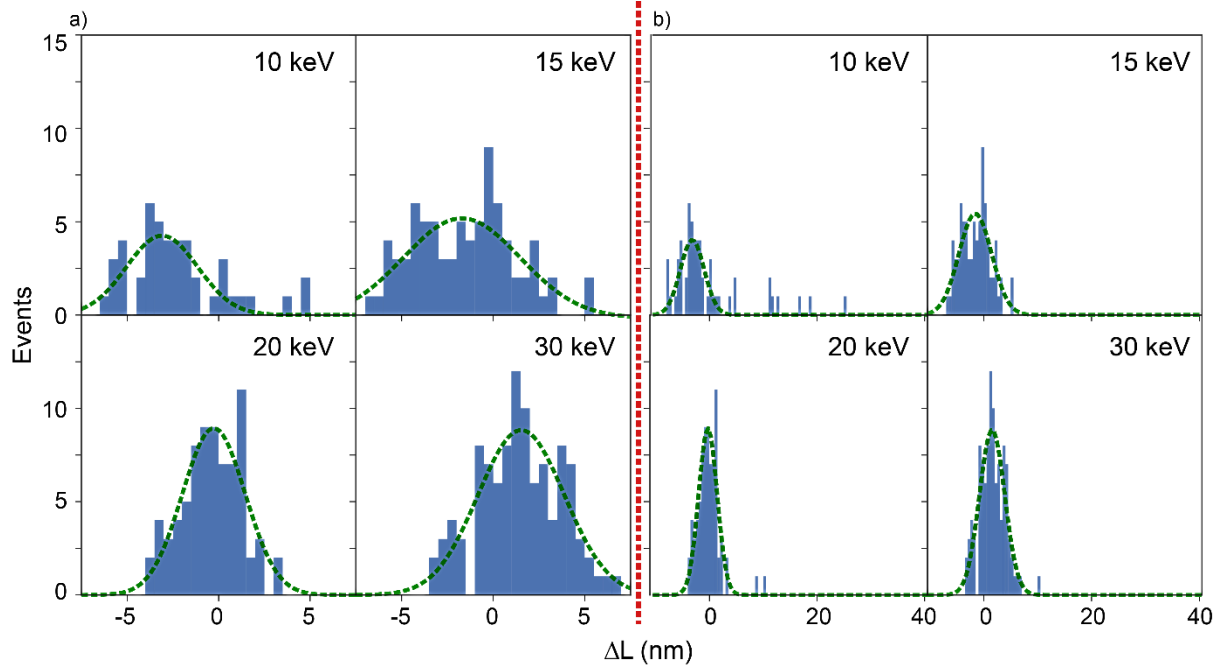


Figure 18 Distribution of ΔL (a) with filtering step 6 and (b) without. The green dashed lines are Gaussians that are fitted through the bins.

BEAM ENERGY (KEV)	FIT VALUES OF GAUSSIAN							
	With filtering step 6				without filtering step 6			
	centre	error	Spread	error	centre	error	Spread	error
10	-3.09	0.30	1.94	0.31	-3.17	0.21	2.22	0.21
15	-1.71	0.38	3.19	0.41	-1.60	0.18	3.03	0.18
20	-0.26	0.15	1.72	0.15	-0.26	0.08	1.72	0.08
30	1.53	0.22	2.36	0.23	1.53	0.11	2.35	0.11

2.5.4 Simplified model

The simplified model is also based on Figure 10 but treats the detection from secondary electrons that escape through the top and side facet independently:

$$I_{SE}(x) = N_{top} * I_{top}(x) + N_{sides} * I_{sides}(x)$$

Here N_{top} and N_{sides} are scaling factors for an electron escaping through the top/side respectively. The intensity from the top and side modes is given by $I_{top}(x)$ and $I_{sides}(x)$. For $I_{top}(x)$ we first assume a homogenous escape probability through the top facet, which is modelled by the multiplication of two step functions. Next, this rectangular escape probability is convoluted with a Gaussian, representing the position uncertainty, which transforms the step functions into cumulative normal distribution functions (CDF):

$$I_{top}(x) = \text{CDF}\left(\frac{x - e_l}{\sigma_u}\right) * \left(1 - \text{CDF}\left(\frac{x - e_r}{\sigma_u}\right)\right)$$

Here e_l and e_r , the left and right edge, are the centres of the two CDF which both have standard deviation σ_u , the position uncertainty. We approximate the contribution from SE that escape through the side facet to the total SE signal by only considering the case when the beam is centred directly on the edge. The spatial spread of SE generation is again assumed to be a normal distribution. Because an SE cannot be generated outside of the cube, we multiply this by an inverse step function. For the left edge this becomes:

$$I_{left_edge}(x) = \exp\left(-\frac{(x - e_l)^2}{\sigma_p^2}\right) * \text{step}(x - e_l)$$

Where σ_p is the spread of the SE production and $\text{step}(x)$ is 1 if x is positive and 0 otherwise. This can be approximated by a skewed normal distribution function (SDF) which has the advantage of being smooth. Doing this for both sides yields a total contribution from the sides of:

$$I_{sides}(x) = \text{SDF}\left(\frac{x - e_l}{\sigma_p}, skew\right) + \text{SDF}\left(\frac{x - e_r}{\sigma_p}, -skew\right)$$

Where $skew$ is the skewness of the SDF, which was constrained to be above 5, and the other parameters are as defined above. This model was then used to filter the measurements as outlined above.

2.6 PROMISES OF A BETTER PRECISION

In Figure 19 the data of the histograms of Figure 5 is displayed in the form of a scatter plot. For each measurement, the difference between the CL and SE models on the left vs the right edge. This difference is defined in Figure 5. The marker indicates at which beam energy the measurement was taken, and the colour represents the measurement set. That is, all measurements of the same colour were done on the same cube. The exception to this rule is the black markers which were all taken on different cubes. What is noteworthy is that if there is a difference between the SE and CL model on one edge it is often also found on the other side. This indicates that whatever causes the difference between the SE and CL data, it affects the cube as a whole. Furthermore, a similar offset is often also found in other measurements on the same cube. The precision of a single measurement set is thus better than the 5 nm of all the measurements taken together. The cause of these offsets that affect the whole cube could be a small layer of carbon deposition or a minor rotation.

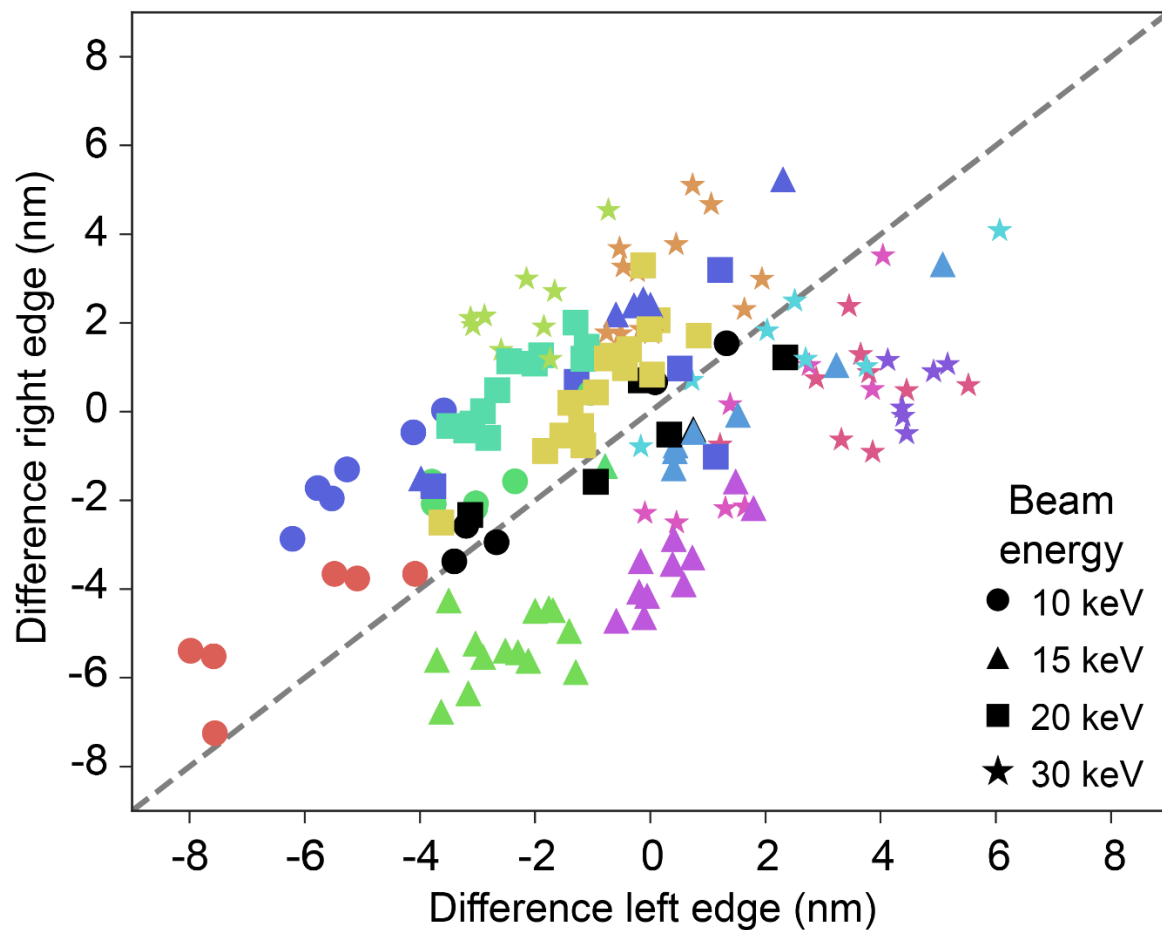


Figure 19 Scatter plot of the difference between where the SE and CL models find the edge. The difference is defined in such a way that it is positive if the cube width as calculated by the CL model is wider than in SE. The shape of the marker represents the beam energy at which the measurement was taken. All measurements with the same colour were done on the same cube except the black markers, which were all done on different cubes. The closer a marker is to the diagonal dashed line, the better the agreement between the left and right edges. 7 cubes fall outside of this plot.

3 DISCOVERING DEFECTS IN A GREEN LED

3.1 INTRODUCTION

Light emitting diodes (LEDs) can be used in a wide variety of different lighting applications such as lamps, screens and lasers. The main advantages of LED's over conventional lighting are their high brightness, efficiency, and long stable operating lifetime⁵⁵. These advantages make LEDs attractive from a commercial standpoint as well as an ecological one. The research on LEDs started in 1907 when H. J. Round observed electroluminescence after applying a current over a semiconductor⁵⁶. In 1927 O.V. Lossev used this principle to build the first functional LED⁵⁷. The research increased in intensity in the 40s and 50s when semiconductor physics became more prominent. This led to the discovery of a red $Ga(As_{1-x}P_x)$ based LED in 1962 by N. Holonyak⁵⁸ and resulted in the first commercial LED which was produced in 1968 by Monsanto. These early LED's were very expensive, but the cost dramatically dropped over the next couple decennia due to improved production techniques and economy of scale. However, even with the combined effort of industry and academia, it was not until 1993 that S. Nakamura created a blue LED. This blue LED was made of a $InGaN/AlGaN$ double-heterostructure¹⁹. Since then many LEDs have been developed but, so far, none that efficiently emits in the green-amber region. This phenomenon, called the green gap⁵⁹, is due to a lack of suitable materials with a direct bandgap for these wavelengths. One way to circumvent the green gap is by down conversion of highly energetic photons. This process is generally done by placing green (and sometimes also red) phosphors in front of a blue LED. The blue photons excite the phosphors which subsequently emit light at a lower wavelength, the remainder energy being lost to heat⁵⁶. While this process can produce RGB light, it induces an extra loss, thereby stripping the LED of one of its key advantages.

One possible material for a green LED is an alloy of $Al_xIn_{1-x}P$. This is because this alloy has a bandgap that is tuneable between 2.45 and 1.34 eV, depending on the Al/In concentration^{60,61}. For efficient light generation it is crucial that this bandgap is direct, something that can be achieved by engineering the crystal symmetry⁶². This is possible for nanowires which have the added benefits of efficient light outcoupling and often need less material to achieve equivalent performance to bulk devices⁶³. Luca Gagliano, from the TUE, designed Wurtzite $Al_xIn_{1-x}P$ nanowires (NW) with varying Al/In concentrations, that emit in the green gap. These NW's consist of a core-shell structure and are grown on an InP substrate⁶⁴. Figure 20 a) shows a schematic of the top of an NW with a 25% Al concentration and b) shows a tilted SE image of a typical example. This core-shell structure is a result of the NW growth process and is visible in Figure 20 c and d). The NW core grows first and expands upwards until it starts to converge again and from a tip. Then the shell is nucleated at the top rim and grows around the NW. Figure 20 c and d show cross lamella perpendicular and parallel to the NW growth direction respectively.

Figure 20 g shows the Photoluminescence (PL) spectra of wires with different Al concentrations. These spectra clearly exhibit the desired bandgap peak, as well as unexpected and unwanted secondary transitions. Paramount to further improving the performance of these NWs was determining the origin of these secondary transitions. Due to the small spatial dimensions of the nanowires, localizing the origin of this luminescence signal was not possible with PL. Cathodoluminescence (CL) is the perfect tool to answer this question because it can obtain CL spectra from the NW regions. For this reason CL is often used to investigate NWs and it has been used to investigate, for example, defects in GaN NWs⁶⁵, plasmons in Ag

NWs²³, or strain in ZnO NWs⁶⁶. We therefore started a collaboration with the goal of using CL to shed light on where in the NW this emission came from and which mechanism was responsible for it. To this end, we investigated two samples, one with an Al concentration of 25% and one with 45% Al. For the sake of clarity, only the results on the nanowire with a 25% Al concentration will be described here. The second sample, with an Al concentration of 45%, displayed the same behaviour but had more atomic defects which resulted in extra luminescence peaks. The investigation of the NW consists of three steps. First the top view of an ensemble of NWs is studied to check the homogeneity of the sample. Then a horizontal NW is scanned to see where in the NW the unwanted secondary peak comes from. Finally, energy-dispersive X-ray spectroscopy is performed on the same horizontal NW to determine the mechanism behind this emission. The results presented in this chapter were published in Nano Letters with the title “Efficient green emission from Wurtzite $Al_xIn_{1-x}P$ nanowires”, (2018)⁶⁴.

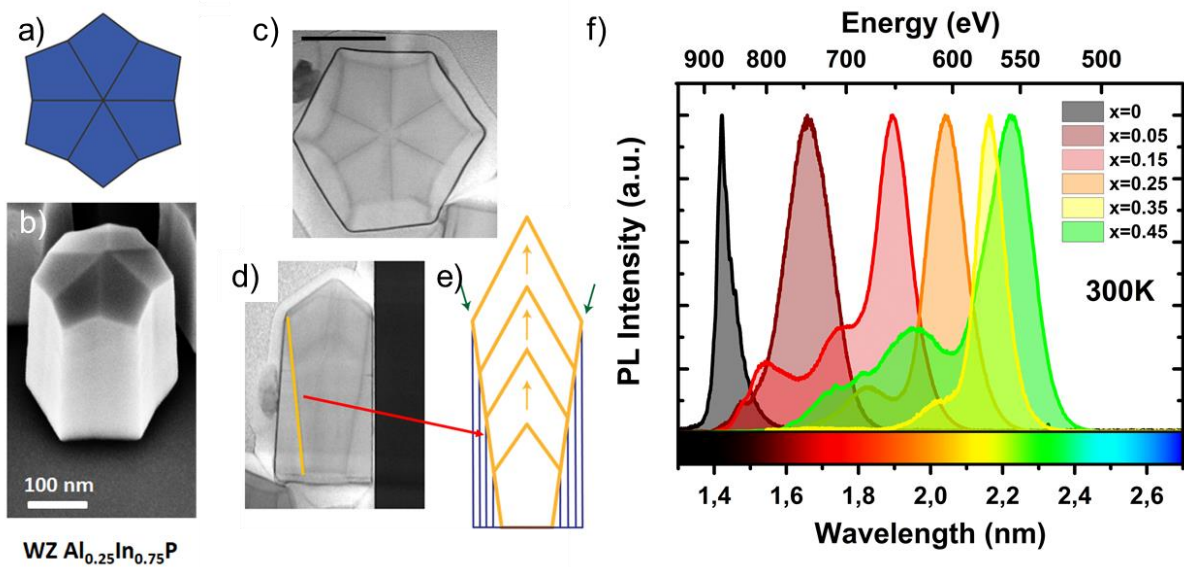


Figure 20 Overview of the Wurtzite nanowires (NW). b-f) study of $Al_{0.25}In_{0.75}P$ NW, (a) schematic of the top facets which can also be seen in (b), which shows a tilted SE image of a typical NW, and compared to (c), a cross lamella with 200 nm scale bar. (d) HAADF-STEM image with the boundary between the core and the shell highlighted in yellow. (e) Displays the growth history of the NW, first the core (yellow) grows, then a shell is nucleated at the rim (green arrows) which then grows around the NW (blue). (g) PL spectra NWs with different $Al_xIn_{1-x}P$ concentrations. Figures are adapted from⁶⁴.

3.2 TOP VIEW

From comparing the different samples, we know that the shape of the nanowires changes with the Al concentration, so any variation in shape is an indication of inhomogeneities in the nanowires. Therefore, the first thing we did was to make an investigation of the top view a nanowires array. Figure 21 a shows the SE view of an array of $Al_{0.25}In_{0.75}P$ nanowires from the top taken with a 2 keV probe. These nanowires have an uniform shape with minor perturbations. A false RGB map of the same nanowires, Figure 21b), shows that these small differences in shape and size do translate to a different emission spectrum. Except for the fourth nanowire in the top row, which is slightly deformed, all NWs emit at similar wavelengths. This consistency underlines the high homogeneity of the sample. The deformed NW has its main peak at 570 nm while the rest of the NWs have theirs around 600 nm, see the average spectra in Figure 21 c and d. Judging from Figure 20 this could indicate that the deformed NW has an Al concentration which is a couple percent lower than that of the other NW. Besides the main, peak all NWs

show a smaller second peak around 675 nm. Both peaks are also observed in the corresponding PL spectra of Figure 20 which exhibits two main peaks, one centred at 600 nm and one at 675 nm.

Figure 21 e and f show the CL intensity within a 50 nm wide band with around the two observed peaks. From these two CL maps, one can deduce multiple conclusions about the homogeneity of the sample and the origin of the different parts of the spectra. First of all, both maps show localized bright spots. We attribute these spots to very localized alloy fluctuations that formed during the NW growth⁶⁷. Secondly, we observe that the two different peaks come from different regions of the NW. The main peak comes from the core while the secondary peak comes from the shell. To test this hypothesis, we will investigate an NW laying on its side in the next chapter. Furthermore, we observe that the core of the deformed NW does not exhibit the same brightness as the rest of the array while the shell does. This implies that the origin of the deformation occurred during the growth of the core and not during that of the shell. Finally, in Figure 21 b and f the NWs have dark lines which coincide with the edges between the different facets, see Figure 20 a. It has recently been proven that this is not due to a different composition, but rather due to a lower excitation efficiency which leads to a lower CL signal⁶⁸.

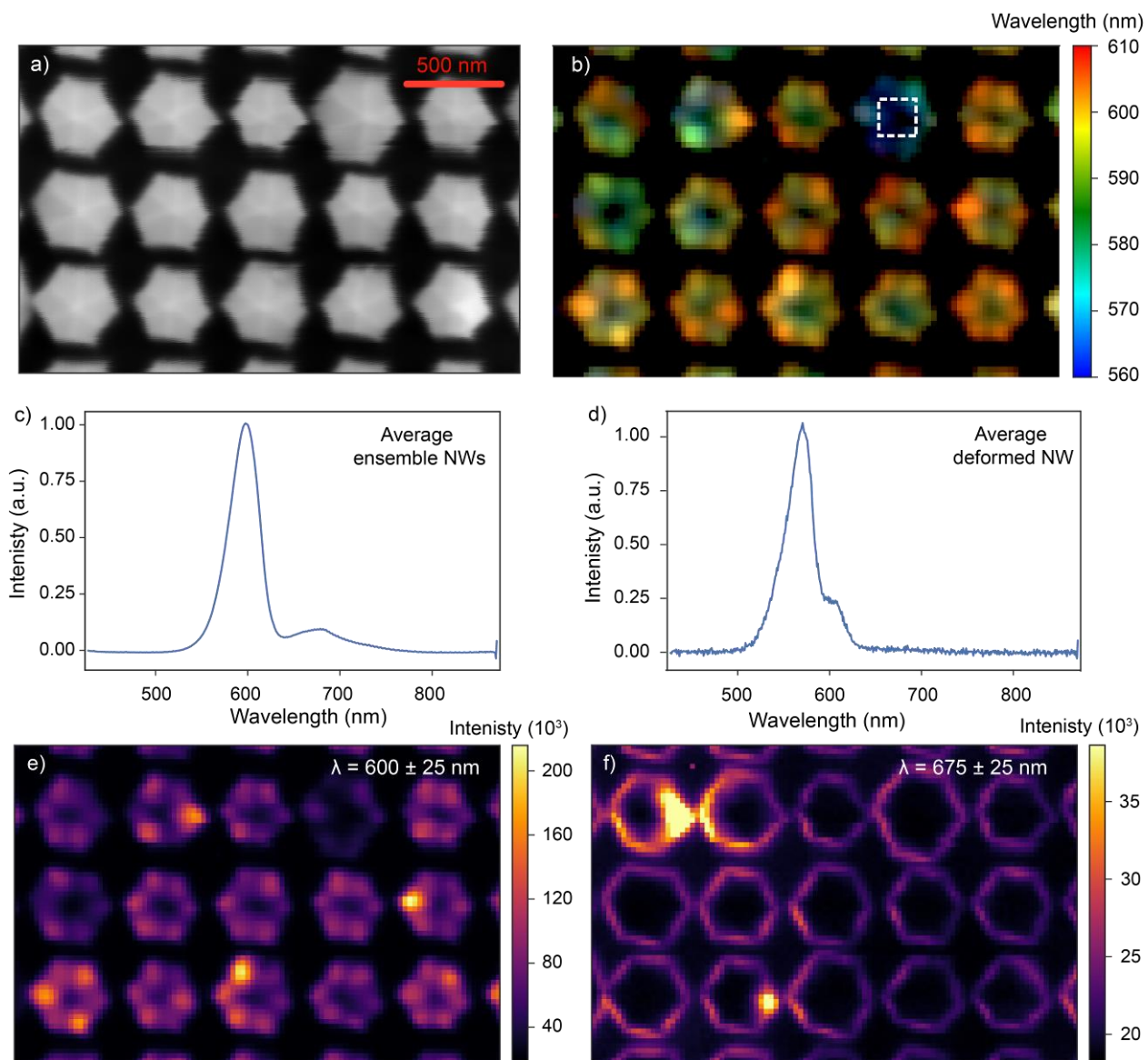


Figure 21 Study of an array of nanowires at 2 keV. **(a)** SEM image of the nanowires **(b)** False-colour RGB map made by separating each spectrum into 3 sections which are then normalized to create an RGB code. **(c)** Spectrum of all the nanowires. **(d)** Spectrum of the cube in **(b)** which is an NW with a slightly different composition. **(e)** and **(f)** maps of the summed CL intensity within a 50 nm bandwidth.

3.3 STUDY OF THE SIDE VIEW OF SINGLE NANOWIRE

To further investigate the origin of the second peak we examined multiple horizontal NWs that were mechanically displaced using a nanomanipulator, of which Figure 22 a is a typical example. Figure 22 b shows the spectra collection along the growth direction on the teal line as a function of the wavelength. The spectra were taken at 5 keV with 0.5 nA. At the bottom of the nanowire, we observed two peaks, which correspond to the core and shell luminescence seen in Figure 21 e and f, while only one peak was visible near the top. Furthermore, both peaks seem to blueshift along the growth direction. To better visualize the evolution of these peaks, each spectrum was fitted with two Gaussians, one for the core and one for the shell. The centres of these Gaussians are plotted as dots in Figure 22 b, with a dashed line drawn through them. These lines exhibit two noteworthy features. First of all, the shell luminescence disappears near the tip of the NW. This can be explained by realizing that the shell disappears near the top of the NW, see Figure 20 d and e. Less trivial is the blueshift along the growth direction that is exhibited by both peaks. The core luminescence shifts from 640 to 600 nm while the centre of the shell emission peak shifts from 730 to 615 nm. The core luminescence near the tip coincides with that observed in Figure 21 e proving that the main peak of the PL spectra in Figure 20 f comes from the emission of the core, near the tip. Based on Figure 21 f and Figure 22 b the secondary peak comes from the shell, about midway along the growth direction of the NW.

There are two possible explanations for the observed shift in the luminescence peaks, strain or an alloy gradient. If a change in the Al concentration is responsible for the spectral shift, Figure 20 can be used to approximate the required change in the Al concentration to account for it. Near the tip, the emission from the core corresponds to an Al concentration of 25% while the core emission near the bottom corresponds to an Al concentration of 15%. This change is more substantial for the shell which decreases from ~20-25% to 5%. To confirm that this is indeed due to an Al gradient along the growth direction we performed EDX on the same NW, which is presented in the next section.

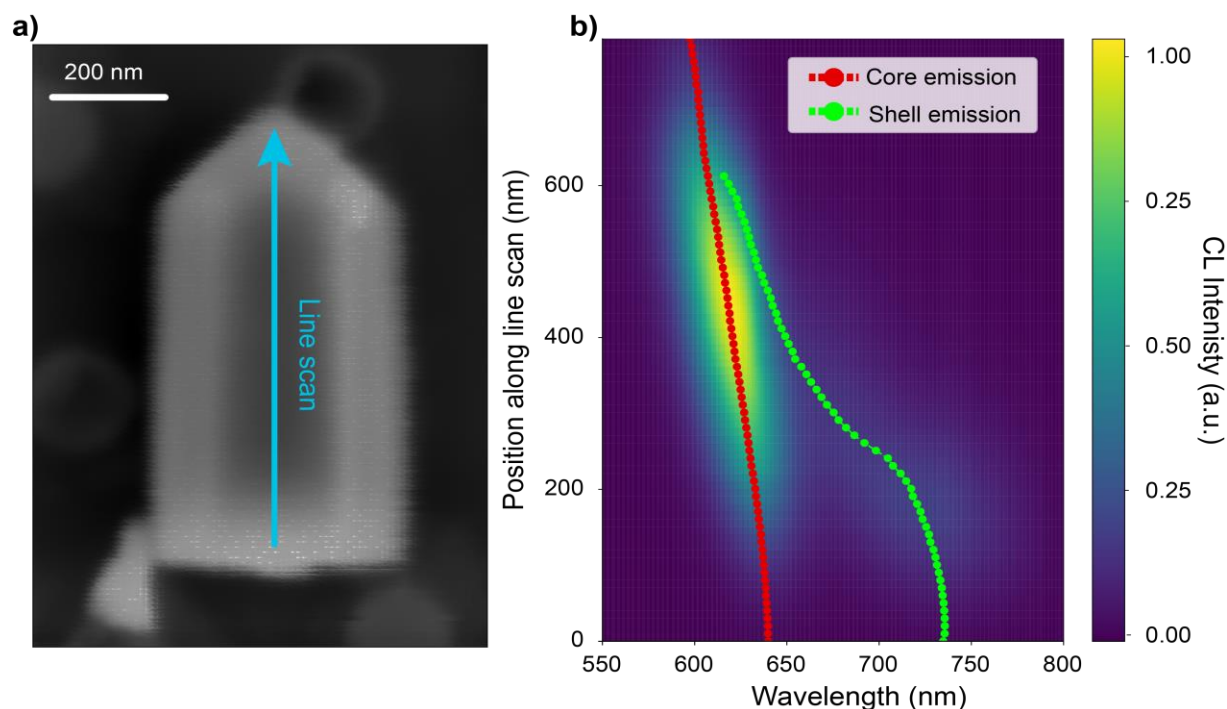


Figure 22 CL scan along the growth direction of NW. **(a)** SEM image that was taken at the same time the CL spectra of **(b)**. The CL spectra of **b)** were taken at 5 keV along the arrow on **a)** which indicates the growth direction. The spectra are fitted with two Gaussians, corresponding to emission from the core and the shell. The periodic oscillations in the spectra above 700 nm are an artefact caused by etaloning in the back-illuminated CCD.

3.4 EDX ON HORIZONTAL NW

To confirm that the aluminium concentration changed along the NW of Figure 22, we performed EDX on it. This EDX was done with a Verios G4 XHR SEM with the help of Andries Lof, at AMOLF. Figure 23 a shows a high-resolution SEM image, that was made in this microscope, of the NW also studied in Figure 22. In EDX an electron beam is sent to a sample where it ejects electrons from the (inner) shells of the atoms. The resulting electron vacancies are subsequently filled by an electron from a higher band while emitting a characteristic X-ray to account for the lower energy of the inner band. In Figure 23 b, an EDX map of the number of Al counts is presented. To improve the signal to noise ratio, the 10 pixels between the two red lines are summed in the x-direction as well as 5 pixels in the y-direction. The resulting line graph can be seen in Figure 23 c where the light/dark green lines are drawn at the same position as in Figure 23 b and roughly correspond to the bottom/tip of the nanowire. From this graph, it is evident that the Al concentration increases along the growth direction.

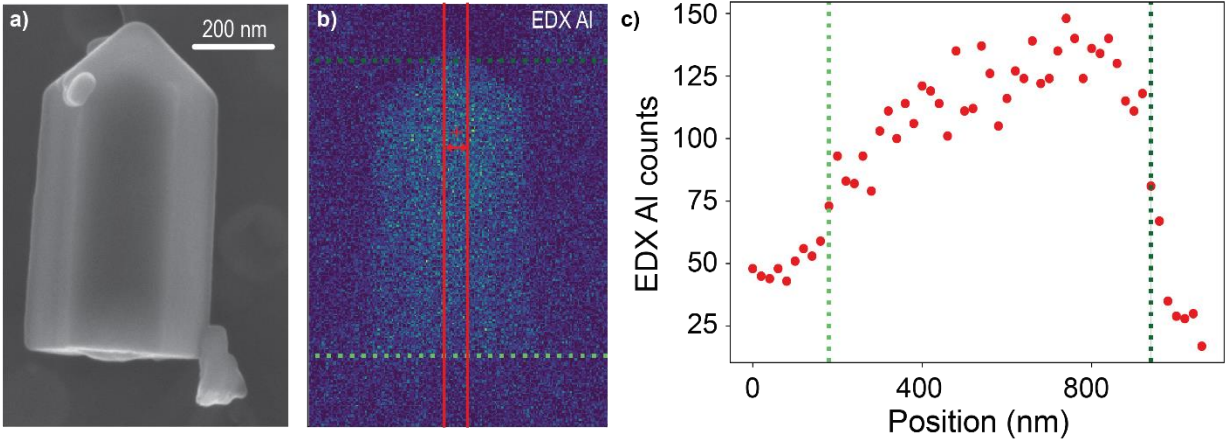


Figure 23 EDX analysis of NW **(a)** High-resolution SEM image of the NW studied in Figure 22. **(b)** EDX map, taken at an acceleration voltage of 5 keV, of the Al concentration on the NW of a). The EDX counts between the two red lines are summed in the x-direction (10 pixels) as well as 5 pixels in the y-direction, yielding the line graph of **(c)** The light/dark green lines in c) correspond to the lines of the same colour in b) and indicate the bottom/tip of the nanowire.

3.5 CONCLUSION

Wurtzite $Al_xIn_{1-x}P$ nanowires show strong potential as LEDs with a direct bandgap that can be tuned between 2.45 and 1.34 eV, making them an excellent candidate to bridge the green gap. However, the first-generation NWs not only exhibited the desired bandgap luminescence but also an unwanted second peak from an unknown origin. Understanding the origin of this peak is crucial for remedying its negative impact on the NW performance. Utilising CL maps of an NW array, we determined that the second emission peak comes from the shell of the NW while the desired bandgap luminescence comes from the core. From a horizontally displaced NW, it could be seen that the luminescence peak of both the core and the shell blueshift across the growth direction. EDX measurements on the same NW suggested that this is due to a gradient in the Al concentration.

4 GRAIN BOUNDARY OF DEGRADED MULTI-CRYSTALLINE SILICON SOLAR CELL

4.1 INTRODUCTION

During its operational lifetime, the efficiency of silicon solar cells slowly decreases. This decrease is due to a variety of processes including cracking⁶⁹, encapsulate decoloration⁷⁰, and light-induced degradation (LID)⁷¹. LID occurs when excess carriers are injected above the bandgap by either solar/artificial illumination above the bandgap⁷², forward biasing⁷³ or temperature⁷⁴. One of the most common degradation mechanisms, and the one studied here, is boron-oxygen LID (BO-LID)⁷¹. Indeed, in 2002 90% of the Silicon solar cell market was based on boron-doped crystalline silicon, showing that the potential impact of a solution to prevent degradation could be huge⁷⁵. The exact mechanism behind BO-LID is unknown, but the consensus is that it is caused by metastable boron–oxygen-related defects that become active recombination centres⁷⁶. This degradation occurs on two different timescales depending on the configuration of the $B_sO_{2i}^1$ complex⁷⁷. The slow decay, due to a square B_sO_{2i} configuration (B-O), typically occurs on a timescale of hours. The fast decay, caused by a staggered configuration (B-Vacancy-O), occurs on a time scale of seconds to minutes. This means that, unless a solar cell has been degenerated and regenerated previously, any solar cell that is susceptible to LID can be considered to be degraded from within the first moment of solar irradiation. A better understanding of the cause of this degradation could help to prevent it, which would increase the average efficiency of boron-doped Silicon solar cells by around 1%⁷⁸.

There are two possible approaches to limiting the adverse effects of LID, limiting the formation/activation of the BO defects or deactivating them after they are formed. This latter process is called regeneration, and it is postulated that it is caused by hydrogen which pacifies the BO defect, thereby deactivating capacity as a recombination site⁷⁹. After a degraded cell is regenerated, it should have regained most of its lost efficiency. A regenerated cell can destabilize and degrade again, but this effect is estimated to take many decades⁷⁶. By choosing the right temperature and hydrogen concentration⁸⁰, it is possible to regenerate the cell in 10s, which would make it possible to degrade and subsequently regenerate a solar cell as part of the production line. Nevertheless, it would be preferable to stop LID from occurring in the first place. For this, a better understanding of the mechanisms at play is needed which could also further improve the regeneration process.

4.2 OUTLINE AND EXPERIMENTAL SETUP

In this chapter, I will show a preliminary investigation of a degraded and undegraded multi-crystalline Silicon solar cell using cathodoluminescence (CL). The solar cell was produced commercially and prepared by Msc. Robert Lee Chin from UNSW. The cell was divided into multiple samples and, for some, the surface passivation was etched away. Afterwards, some of these samples were degraded by placing them on a hotplate under illumination of an 800 nm high-power laser. After a short burst of this treatment, the lifetime was measured, and the process was repeated. This way the average minority carrier lifetime degraded from 80 μ s to 20 μ s.

¹ B_s stand for is substitutional boron and O_i for interstitial oxygen.

Here I will present the results of the etched samples on which we measured the total brightness and the bandgap luminescence. To stop the degraded sample from regenerating, we cooled it using liquid nitrogen to roughly 120 K. An SE image from the cooled undegraded sample can be seen in Figure 24 a and shows a regular pattern on the surface. This pattern is not visible at room temperature, and we postulate that it is caused by residue of the anti-reflection coating that remained after etching. Since it did not seem to influence the CL spectra, it was not investigated further. Figure 24 b shows typical spectra of the bulk that were taken >100 μm away from the nearest grain boundary. These spectra, as well as all other CL data used in this chapter, are after dark count subtraction and correction for the system response. The correction for the system response was very sensitive to noise in the lower wavelength regime due to the low detection efficiency. To counter the effect of noise in this region the minimum of each spectrum was set to zero. Furthermore, all spectra are normalised to enable the comparison of areas with different CL intensity and experimental parameters. The resulting spectra of Figure 24 b) clearly show a peak around 1120 nm, which corresponds to the Silicon bandgap. There also appears to be some sup-bandgap luminescence from 1150 till 1450 nm. This could be due to a combination of displacement peaks and defects⁸¹. For the first spectra of the degraded sample, especially the D2 displacement peak, at 1440 nm, is visible. In this chapter, the origin of this luminescence will be investigated as well as whether it is stronger near the grain boundary. To this end, we compare the total CL signal and the relative intensity of the bandgap peak, I_{bg} , taken close to and far from the bandgap for each sample. The former is calculated by summing all photons in the range 1050-1450 nm. The second measure of interest is the relative intensity of the bandgap luminescence. This is calculated by averaging the CL intensity between 1120 and 1125 nm, normalized by the total CL intensity.

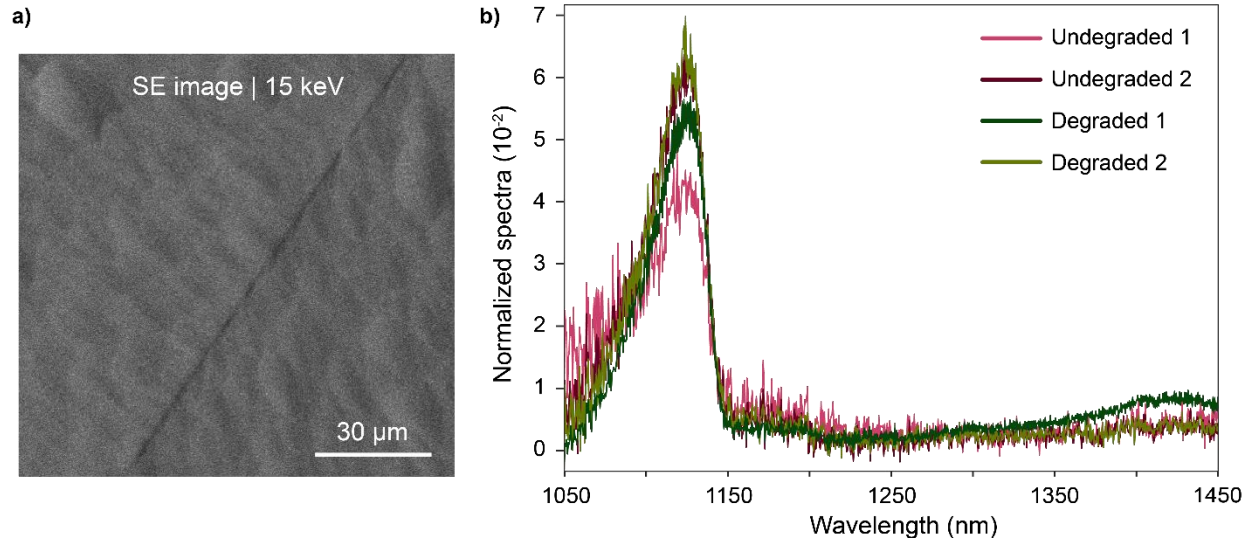


Figure 24 Sample image and example spectra (a) four normalised spectra which were measured at different points on the two different samples. All scans were taken at high currents (90-140nA) and 15 keV (b) SE image of grain boundary on the degraded sample at a cooled temperature.

4.3 CURRENT-DEPENDENT REGENERATION TEST

To test whether the degraded sample was regenerating under electron irradiation, we performed two measurements, one with a current of 5 nA and one with 140 nA, shown in

Figure 25. For the 5 nA test, we took one CL spectra every minute for 16 minutes. While the CL intensity of this test does not show a noticeable change, the relative bandgap luminescence, as defined in the previous section, does seem to decrease. This decrease is especially visible in the 140 nA scan in which we took a CL spectrum every five seconds for 6 minutes. At the end of the scans the relative bandgap intensity has decreased by 5-10% while the CL intensity hardly changes. The origin of these observations is unclear because both are opposite of what is expected for a sample that is regenerating. In a regenerated sample the BO recombination sites are inactive, just as in an undegraded sample. A regenerating sample should thus show an increasing CL intensity and bandgap luminescence. An alternative explanation could be carbon deposition, which was visible after all high current scans. This carbon deposition could form a barrier for the photons, decreasing their detection probability. However, this would not adequately explain why the bandgap luminescence is reduced while the total intensity is unaffected. Whatever the process is that is behind the observed change is thus most likely something that influences the material properties in a more complicated way than carbon deposition.

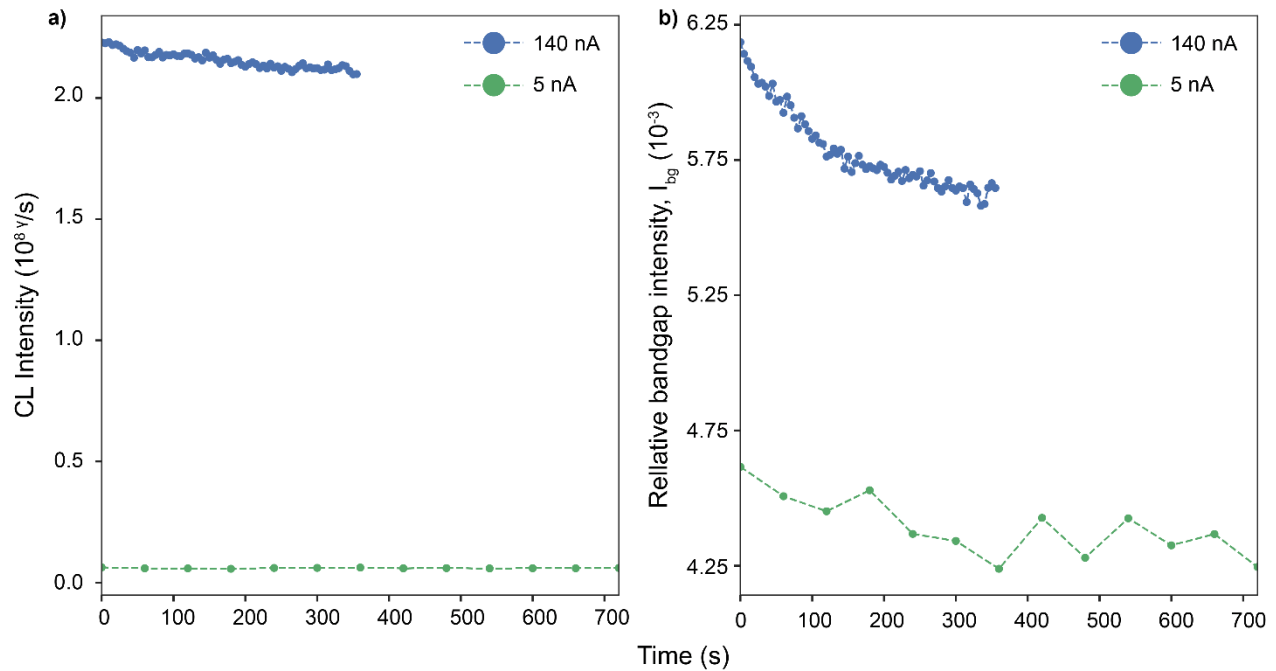


Figure 25 Two different tests to see if the influence of the electron beam was strong enough to regenerate the degraded sample. For both tests, a 15 keV electron beam is focused on a single point and spectra are taken with 5 nA (one spectra every minute for 16 minutes) and 140 nA (one spectrum recorded every 5 seconds for 6 minutes). (a) The CL intensity, defined as is the total number of photons that were emitted in the 1050-1450 nm range of both measurements and (b) the relative bandgap intensity, the average value of the spectrum in the 1120-1125 range, normalised by the total CL intensity.

Based on these tests we concluded that regeneration, or whichever process is responsible for the spectral changes, should not have a significant influence on the experiments for two reasons. Firstly, the variations observable in this test are relatively small, on the order of 5-10%. This is much less than the differences across the grain boundary, which are detailed in the following section and are around 30%. Secondly, the time a measured area was part of the region of interaction of the electron beam was much shorter during

all other experiments than during the current test. The measurements had an acquisition time between 2-10s and a minimum step size of 1.5 μm . That means that even for the 30 keV electron beam, which has a region of interaction of around 3.5 μm , the maximum time an area was affected during experiments was around one minute. This is significantly shorter than the 6 minutes of the for the 150 nA and 15 minutes for the 5 nA current test.

4.4 VARIATION ALONG THE GRAIN BOUNDARY

During the measurements of the undegraded and degraded samples, we observed a lot of change in the CL intensity and bandgap luminescence depending on the position on the samples. This variation was also seen along the grain boundary, as shown in Figure 26. This implies that there is some variation of the material properties on the same length scale as the effect of the grain boundary is visible. Therefore, in the next sections, the relative change of the spectral properties warrants more attention than the absolute value.

Figure 26 b shows the SE contrast acquired on the undegraded sample, with the grain boundary indicated with a dashed line, at the same time that the CL maps were measured. Figure 26 a shows the total CL intensity and c shows the relative peak intensity as defined in the introduction. Figure 26 d-f presents the same investigation as Figure 26 a - c but then on the degraded sample. The two scans are taken at different acceleration energies, which explains the worse resolution of Figure 26) when compared to e, as well as its higher CL signal. This is because the region of interaction is 3.5 μm across for a 30 keV beam and 1 μm for a 15 keV beam. The fact that the variance was found on all samples independent of the beam parameters confirms that it is due to fluctuations of the material properties. The cause of this variation is unknown and reacquires further investigation. Interestingly, the CL intensity, Figure 2 a and d, and the relative bandgap intensity, c and f, of both graphs seems to be inversely correlated. Indicating that an increase in the CL intensity is more due to a rise in the sub-bandgap luminescence than that of the bandgap. This can be seen in Figure 27, which shows four normalised spectra taken at points with a high and low relative bandgap luminescence on both samples. Here it can indeed be seen that in area's with a high CL intensity, the sub-bandgap luminescence increases more than the bandgap luminescence. This sub-bandgap luminescence does not show any clear peaks but is rather homogeneous over the measured spectral range.

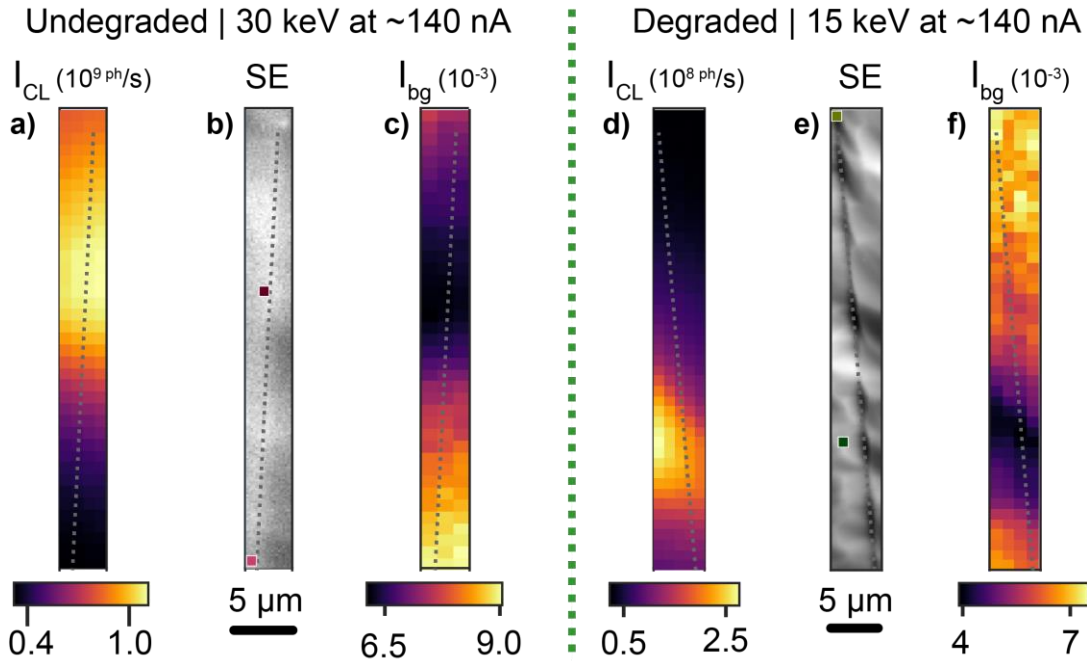


Figure 26 Comparison of the CL signal along a grain boundary for both undegraded and degraded samples. (a) and (d) SE contrast taken at the same time as the CL image with grain boundary indicated by a thin dashed line. Figure 27 shows the spectra taken at the coloured squares. (b) and (e) Total CL intensity along the grain boundary. (c) and (f) Relative peak intensity along the grain boundary.

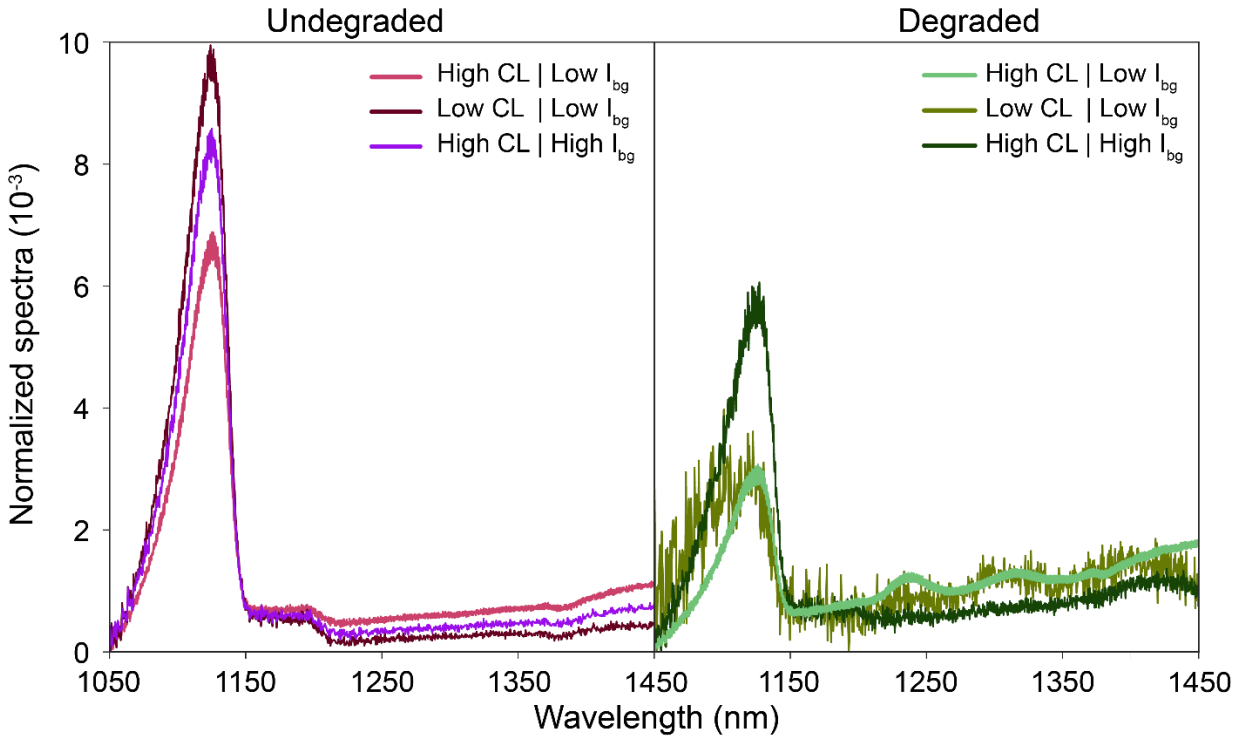


Figure 27 normalised spectrum taken at ~140 nA on two different samples, the spectra on the undegraded sample were made at 30 keV, and the degraded spectra at 15 keV. For each sample, one spectrum is taken from an area with high CL intensity, and low relative bandgap luminescence and another from an area where the CL intensity was low and the bandgap luminescence relatively strong, these areas are indicated in Figure 26.

4.5 VARIATION PERPENDICULAR TO THE GRAIN BOUNDARY

To investigate how the degradation influences the CL spectra near the grain boundaries we performed multiple scans perpendicular to it. Figure 28 shows two examples of such scans taken on the undegraded sample at different acceleration voltages, 30 and 15 keV, with the same current. The measurement shown in Figure 5 a-d was taken at 30 keV and, just as the measurements along the grain boundary, exhibits a non-uniform CL intensity and relative strength of the bandgap luminescence. To be less sensitive to the variation along the grain boundary, we averaged the bandgap luminescence over the pixels parallel to the grain boundary. This yields a single value per position perpendicular to the grain boundary, Figure 28 d. From this, it is clear that the relative strength of the bandgap luminescence decreases close to the grain boundary, while the total CL intensity increases. This indicates that the sub-bandgap luminescence from defects grows more strongly than the bandgap luminescence. The second example, Figure 28 e-h, shows a scan taken over an area further away from the grain boundary. Here the grain boundary has the same influence on the CL spectrum as in a-d. That is, both the sub-wavelength luminescence and the bandgap luminescence go up near the grain boundary, but the sub-bandgap luminescence goes up more yielding a relatively lower bandgap peak intensity. Besides the dip due to the grain boundary, a second dip is visible 15 μm right of the grain boundary. This second dip could be caused by another grain boundary which lays just below the surface. Because this scan extends over a larger area, we can also see that the length over which the grain boundary influences the measurement is around 20 μm .

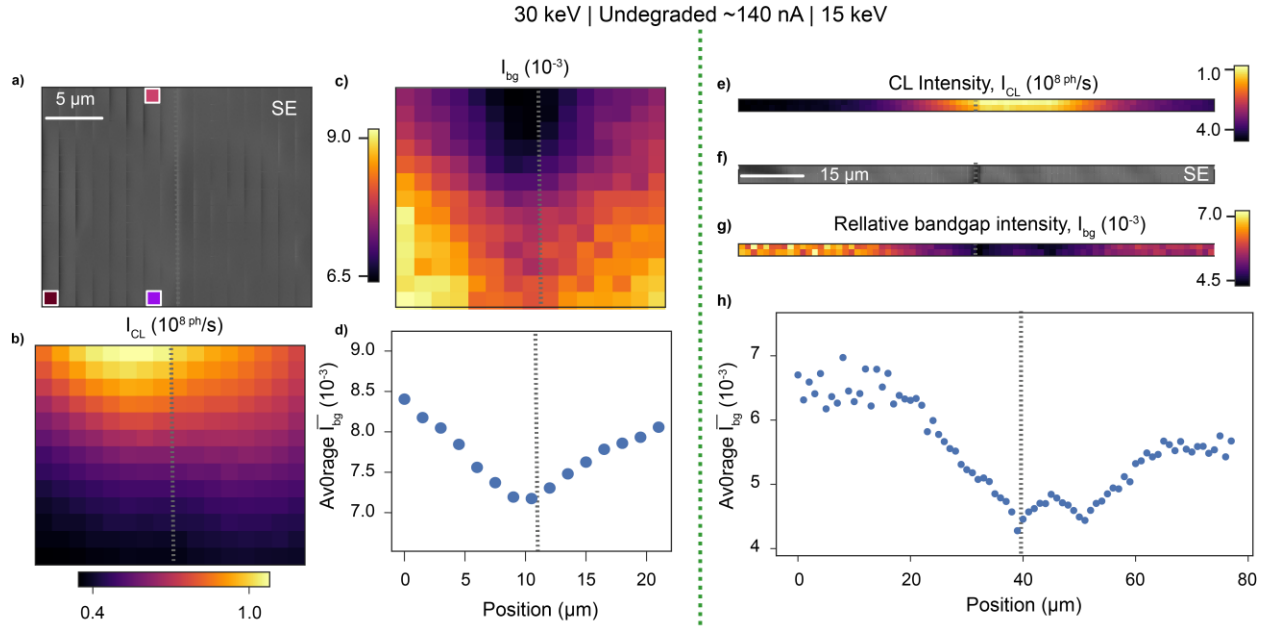


Figure 28 Two scans across different locations on the same grain boundary of the undegraded sample with the same current at different beam energies. (a) and (e) SE image taken at the same time as the CL signal. Grey dashed line indicates the grain boundary and the coloured cubes are where the spectra in Figure 30 are taken. (b) and (f) CL intensity. (c) and (g) Intensity of the bandgap peak normalised by the total CL intensity. d and h) Relative peak intensity, of c and g respectively, averaged over the height of the scan.

Next, the investigation presented in Figure 28 was performed on the degraded sample, see Figure 29. Here we kept the acceleration current at 15 keV because the region of interaction at this energy is more than three times smaller than at 30 keV, which results in a higher spatial resolution. In the first scan, Figure 29 a-d, the CL intensity goes up close to the edge due to a rise in the bandgap luminescence and an even

stronger increase of the sub-bandgap luminescence, just as in Figure 28. Unlike Figure 28, the relative peak intensity does not go up far away from the grain boundary. It instead seems to go down continuously from left to right with an extra dip from the grain boundary. This continuous decline is also visible in the second scan, right column of Figure 29, but here the effect of the grain boundary is not visible. A possible interpretation for this decline is that the sample is regenerating more strongly than anticipated based on Figure 25. While this is possible, it is not a wholly satisfactory explanation for three reasons. First of all, a regenerating sample is expected to display an increasing CL intensity and a rise in the bandgap luminescence, which is opposite of what we observe. Furthermore, $\overline{I_{bg}}$ is averaged over multiple rows which were acquired consecutively. So not every pixel on the right was taken for every pixel on the left. Finally, if the samples were regenerating due to the electron beam, one would expect that regeneration increases in the beginning, as areas spend more time in the region of interaction, and that it evens out afterwards. The regeneration should thus be most visible on a length scale comparable to the region of interaction, which is $1\text{ }\mu\text{m}$ for a 15 keV beam. Neither would carbon deposition or alignment drift be an adequate explanation because the former should not display such a sharp position dependence and the latter should not influence the spectra. This leaves fluctuations of the material properties as the most likely explanation. However, this is all but guaranteed, and more scans over large areas are needed to say for sure.

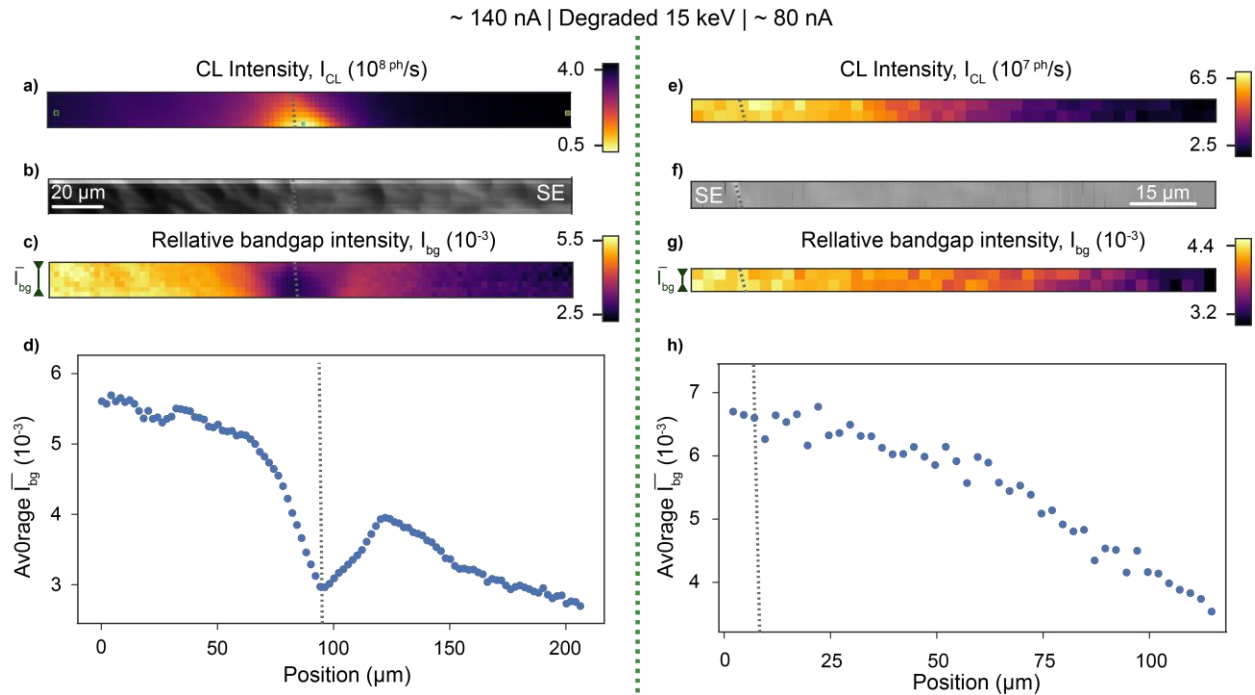


Figure 29 Two scans across different grain boundaries of the degraded sample, with the same beam energies but different currents and integration time (10 and 4 s). b and f) SE image taken at the same time as the CL signal, with grain boundary highlighted with grey dashed line. a and e) CL intensity. c and g) Intensity of the bandgap peak normalised by the total CL intensity. d and h) Relative peak intensity, of c and g respectively, averaged over the height of the scan.

When comparing the CL intensity and relative peak intensity of the four different measurements shown above we see that there is a non-trivial relation between the two. If the CL intensity is relatively high, this is due to an increase in both the bandgap and sub-bandgap luminescence, with the latter increasing relatively more. In Regions where the CL intensity is relatively low, this is again because both bandgap and

sub-bandgap luminescence decrease but here the bandgap emission is more influenced. This could indicate that there are two different phenomena at work. It seems that the mechanism responsible for the increased the CL intensity, affects the defects that cause the sub-bandgap luminescence more strongly than it enhances the radiative decay from the bandgap. When the CL intensity decreases further away from the grain boundary, this is due to another process which reduces the bandgap luminescence until the signal from noise and defects dominates. It is therefore instructive to compare three points for both samples; high CL intensity with either low or high I_{bg} and low CL signal with low I_{bg} . These spectra are shown in Figure 30 where the spectra of the undegraded sample came from the points indicated on the scan in Figure 28 a-d and, the degraded spectra came from the points indicated in the scan of Figure 29 a-d. For the undegraded sample, the sub-bandgap luminescence is broad and does not seem to come from a particular defect. In the degraded sample, however, there are three clear peaks visible in both areas with low I_p , at 1240, 1330, and 1400 nm. These peak positions correspond well to the values given in the literature for the displacement peaks D4 –D2⁸², which are at 1240, 1327, and 1417 nm. Displacement peaks are caused by strain due to partial deformation of the crystal lattice⁸³. Interestingly this is also near the grain boundary where displacements are most expected. However, since these peaks were not observed in the other measurements a more thorough investigation is needed.

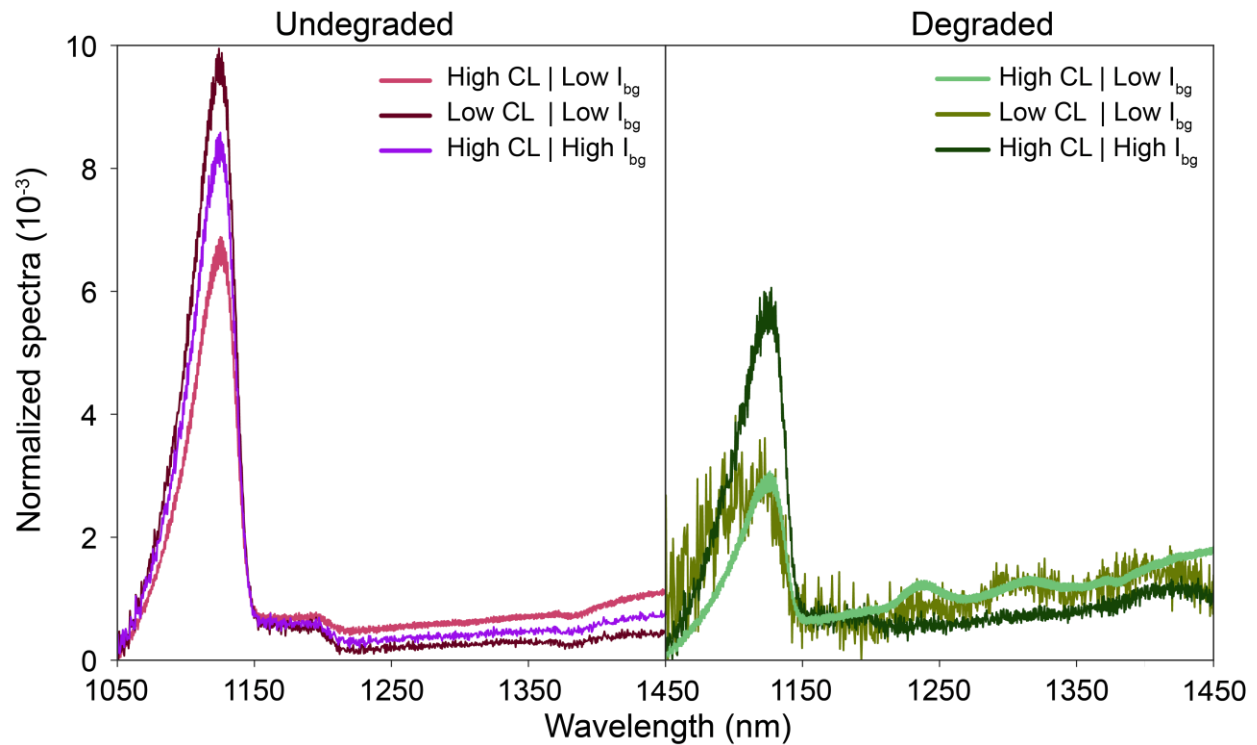


Figure 30 Spectra taken at different points on Figure 28 a) and Figure 29 a). All spectra are normalised and corrected for the spectral response of the camera

4.6 CONCLUSION

In this chapter, a preliminary investigation into how degradation affected the CL signal close to a grain boundary of a multi-crystalline Silicon solar cell is presented. To stop the degraded sample from

regenerating we cooled the sample to 120 K and performed two tests during which we only observed relatively small changes in the spectra. Next, we looked at how the total CL intensity and the relative bandgap luminescence changed along and perpendicular to the grain boundary. During these scans, we observed a significant variation in both the CL intensity and bandgap luminescence. Especially the high variation along the grain boundary, which implies inhomogeneities in the material properties, demands a lot of statistics for a proper analysis. Nevertheless, in most scans, the CL intensity went up close to the bandgap while the relative peak intensity went down. This effect was observed in both the degraded and the undegraded sample. The difference is that both the CL intensity and relative bandgap luminescence were higher in the bulk of the undegraded sample and close to the grain boundaries. Furthermore, in the degraded sample, we observed clear displacement peaks during some of the measurements. However, since they were not found in all degraded scans, this does not rule out that they are also present on the undegraded sample and warrants further investigation. To continue this project, Robert Lee Chin, from UNSW, will visit AMOLF to be trained by me and perform further measurements.

BIBLIOGRAPHY

1. Moore, G. E. Cramming more components onto integrated circuits (Reprinted from Electronics, pg 114-117, April 19, 1965). *Proc. Ieee* **86**, 82–85 (1965).
2. Exchange, E. Processing power compared. 2015 Available at: <https://pages.experts-exchange.com/processing-power-compared>.
3. Yang, X. *et al.* Nanoscale morphology of high-performance polymer solar cells. *Nano Lett.* **5**, 579–583 (2005).
4. Atwater, H. A. & Polman, A. Plasmonics for improved photovoltaic devices. *Nat. Mater.* **9**, 205–213 (2010).
5. Mahian, O., Kianifar, A., Kalogirou, S. A., Pop, I. & Wongwises, S. A review of the applications of nanofluids in solar energy. *Int. J. Heat Mass Transf.* **57**, 582–594 (2013).
6. Singh, R. & Nalwa, H. S. Medical applications of nanoparticles in biological imaging, cell labeling, antimicrobial agents, and anticancer nanodrugs. *J. Biomed. Nanotechnol.* **7**, 489–503 (2011).
7. Eatemadi, A. *et al.* Carbon nanotubes: properties, synthesis, purification, and medical applications. *Nanoscale Res Lett* **9**, 393 (2014).
8. Tan, S. T., Sun, X. W., Demir, H. V. & Denbaars, S. P. Advances in the LED materials and architectures for energy-saving solid-state lighting toward lighting revolution. *IEEE Photonics J.* **4**, 613–619 (2012).
9. Chao, W. *et al.* Real space soft x-ray imaging at 10 nm spatial resolution. *Opt. Express* **20**, 9777 (2012).
10. Suga, M. *et al.* Native structure of photosystem II at 1.95 Å resolution viewed by femtosecond X-ray pulses. *Nature* **517**, 99–103 (2015).
11. Hirata, K. *et al.* Determination of damage-free crystal structure of an X-ray-sensitive protein using an XFEL. *Nat. Methods* **11**, 734–736 (2014).
12. Neutzo, R., Wouts, R., Van Der Spoel, D., Weckert, E. & Hajdu, J. Potential for biomolecular imaging with femtosecond X-ray pulses. *Nature* **406**, 752–757 (2000).
13. Klar, T. A., Jakobs, S., Dyba, M., Egner, A. & Hell, S. W. Fluorescence microscopy with diffraction resolution barrier broken by stimulated emission. *Proc. Natl. Acad. Sci.* **97**, 8206–8210 (2000).
14. Betzig, E., Patterson, G. H. & Sougrat, R. Imaging intracellular fluorescent proteins at nanometer resolution. **313**, 1642–1645 (2006).
15. Mayer, J., Giannuzzi, L. A., Kamino, T. & Michael, J. TEM sample preparation and FIB-induced damage. *MRS Bull.* **32**, 400–407 (2007).
16. García De Abajo, F. J. Optical excitations in electron microscopy. *Rev. Mod. Phys.* **82**, 209–275 (2010).
17. Morishita, S. *et al.* Attainment of 40.5 pm spatial resolution using 300 kV scanning transmission electron microscope equipped with fifth-order aberration corrector. *Microscopy* **67**, 46–50 (2018).
18. Kothleitner, G. *et al.* Quantitative elemental mapping at atomic resolution using X-ray spectroscopy. *Phys. Rev. Lett.* **112**, 1–5 (2014).
19. Nakamura, S., Mukai, T. & Senoh, M. Candela-class high-brightness InGaN/AlGaN double-heterostructure blue-light-emitting diodes. *Appl. Phys. Lett.* **64**, 1687–1689 (1994).
20. Krivanek, O. L. *et al.* Towards sub-10 meV energy resolution STEM-EELS. *J. Phys. Conf. Ser.* **522**, (2014).
21. Crookes, W. On Radiant Matter. *J. Franklin Inst.* **111**, 305–316 (1879).
22. Coenen, T. & Haegel, N. M. Cathodoluminescence for the 21st century: Learning more from light. *Appl. Phys. Rev.* **4**, (2017).

23. Vesseur, E. J. R., De Waele, R., Kuttge, M. & Polman, A. Direct observation of plasmonic modes in Au nanowires using high-resolution cathodoluminescence spectroscopy. *Nano Lett.* **7**, 2843–2846 (2007).
24. Maier, S. a. *Fundamentals and Applications Plasmonics : Fundamentals and Applications. Physics* **677**, (2004).
25. Berini, P. & De Leon, I. Surface plasmon-polariton amplifiers and lasers. *Nat. Photonics* **6**, 16–24 (2012).
26. Ma, R. M., Oulton, R. F., Sorger, V. J. & Zhang, X. Plasmon lasers: Coherent light source at molecular scales. *Laser Photonics Rev.* **7**, 1–21 (2013).
27. Gramotnev, D. K. & Bozhevolnyi, S. I. Plasmonics beyond the diffraction limit. *Nat. Photonics* **4**, 83–91 (2010).
28. Engheta, N., Salandrino, A. & Alù, A. Circuit elements at optical frequencies: Nanoinductors, nanocapacitors, and nanoresistors. *Phys. Rev. Lett.* **95**, 1–4 (2005).
29. Kirchain, R. & Kimerling, L. A roadmap for nanophotonics. *Nat. Photonics* **1**, 303–305 (2007).
30. Kabashin, A. V. *et al.* Plasmonic nanorod metamaterials for biosensing. *Nat. Mater.* **8**, 867–871 (2009).
31. Rossouw, D., Couillard, M., Vickery, J., Kumacheva, E. & Botton, G. A. Multipolar plasmonic resonances in silver nanowire antennas imaged with a subnanometer electron probe. *Nano Lett.* **11**, 1499–1504 (2011).
32. Rossouw, D. & Botton, G. A. Plasmonic response of bent silver nanowires for nanophotonic subwavelength waveguiding. *Phys. Rev. Lett.* **110**, 1–5 (2013).
33. Myroshnychenko, V. *et al.* Plasmon spectroscopy and imaging of individual gold nanodecahedra: A combined optical microscopy, cathodoluminescence, and electron energy-loss spectroscopy study. *Nano Lett.* **12**, 4172–4180 (2012).
34. Coenen, T., Vesseur, E. J. R., Polman, A. & Koenderink, A. F. Directional emission from plasmonic Yagi-Uda antennas probed by angle-resolved cathodoluminescence spectroscopy. *Nano Lett.* **11**, 3779–3784 (2011).
35. Egerton, R. F. *Electron Energy-Loss Spectroscopy in the Electron Microscope*. (Springer Science & Business Media, 2011).
36. Losquin, A. *et al.* Unveiling nanometer scale extinction and scattering phenomena through combined electron energy loss spectroscopy and cathodoluminescence measurements. *Nano Lett.* **15**, 1229–1237 (2015).
37. Das, P., Chini, T. K. & Pond, J. Probing higher order surface plasmon modes on individual truncated tetrahedral gold nanoparticle using cathodoluminescence imaging and spectroscopy combined with FDTD simulations. *J. Phys. Chem. C* **116**, 15610–15619 (2012).
38. Koh, A. L., Fernández-Domínguez, A. I., McComb, D. W., Maier, S. A. & Yang, J. K. W. High-resolution mapping of electron-beam-excited plasmon modes in lithographically defined gold nanostructures. *Nano Lett.* **11**, 1323–1330 (2011).
39. Iberi, V. *et al.* Resonance-Rayleigh scattering and electron energy-loss spectroscopy of silver nanocubes. *J. Phys. Chem. C* **118**, 10254–10262 (2014).
40. Edwards, P. R., Sleith, D., Wark, A. W. & Martin, R. W. Mapping localized surface plasmons within silver nanocubes using cathodoluminescence hyperspectral imaging. *J. Phys. Chem. C* **115**, 14031–14035 (2011).
41. Nicoletti, O. *et al.* Three-dimensional imaging of localized surface plasmon resonances of metal nanoparticles. *Nature* **502**, 80–84 (2013).
42. Demers, H. *et al.* Three-dimensional electron microscopy simulation with the CASINO Monte Carlo software. *Scanning* **33**, 135–146 (2011).
43. Kociak, M. & Zaganel, L. F. Cathodoluminescence in the scanning transmission electron

- microscope. *Ultramicroscopy* **176**, 112–131 (2017).
44. Drouin, D. *et al.* CASINO A Fast and Easy to use Modeling Tool for Scanning Electron Microscopy and Microanalysis. **29**, 92–101 (2007).
 45. Hohenester, U. & Trügler, A. MNPBEM - A Matlab toolbox for the simulation of plasmonic nanoparticles. *Comput. Phys. Commun.* **183**, 370–381 (2012).
 46. Hohenester, U. Simulating electron energy loss spectroscopy with the MNPBEM toolbox. *Comput. Phys. Commun.* **185**, 1177–1187 (2014).
 47. García de Abajo, F. J. & Howie, A. Retarded field calculation of electron energy loss in inhomogeneous dielectrics. *Phys. Rev. B - Condens. Matter Mater. Phys.* **65**, 1154181–11541817 (2002).
 48. Zhang, S., Bao, K., Halas, N. J., Xu, H. & Nordlander, P. Substrate-induced Fano resonances of a plasmonic nanocube: A route to increased-sensitivity localized surface plasmon resonance sensors revealed. *Nano Lett.* **11**, 1657–1663 (2011).
 49. Sun, Y., Yugang Sun, Xia, Y. & Sun, Y. Shape-Controlled Synthesis of Gold and Silver Nanoparticles. *Science (80-.)*. **298**, 2176–2179 (2002).
 50. Waxenegger, J., Trügler, A. & Hohenester, U. Plasmonics simulations with the MNPBEM toolbox: Consideration of substrates and layer structures. *Comput. Phys. Commun.* **193**, 138–150 (2015).
 51. Schmidt, F. P. *et al.* Dark plasmonic breathing modes in silver nanodisks. *Nano Lett.* **12**, 5780–5783 (2012).
 52. Ennos, A. E. The origin of specimen contamination in the electron microscope. *Br. J. Appl. Phys.* **101**, (1953).
 53. Griffiths, A. J. V. & Walther, T. Quantification of carbon contamination under electron beam irradiation in a scanning transmission electron microscope and its suppression by plasma cleaning. *J. Phys. Conf. Ser.* **241**, (2010).
 54. Seager, C. H., Tallant, D. R. & Warren, W. L. Cathodoluminescence, reflectivity changes, and accumulation of graphitic carbon during electron beam aging of phosphors. *J. Appl. Phys.* **82**, 4515–4519 (1997).
 55. Pimputkar, S., Speck, J. S., Denbaars, S. P. & Nakamura, S. Prospects for LED lighting. *Nat. Photonics* **3**, 180–182 (2009).
 56. Tsao, J. Y. *et al.* Toward Smart and Ultra-efficient Solid-State Lighting. *Adv. Opt. Mater.* **2**, 809–836 (2014).
 57. Lossev, O. V. CII. Luminous carborundum detector and detection effect and oscillations with crystals. *London, Edinburgh, Dublin Philos. Mag. J. Sci.* **6**, 1024–1044 (1928).
 58. Holonyak, N. & Bevacqua, S. F. Coherent (visible) light emission from Ga(As_{1-x}P_x) junctions. *Appl. Phys. Lett.* **1**, 82–83 (1962).
 59. Auf Der Maur, M., Pecchia, A., Penazzi, G., Rodrigues, W. & Di Carlo, A. Efficiency Drop in Green InGa_N/Ga_N Light Emitting Diodes: The Role of Random Alloy Fluctuations. *Phys. Rev. Lett.* **116**, 1–5 (2016).
 60. Lorenz, M. R., Chicotka, R., Pettit, G. D. & Dean, P. J. The fundamental absorption edge of AlAs and AlP. *Solid State Commun.* **8**, 693–697 (1970).
 61. Beaudoin, M., DeVries, A. J. G., Johnson, S. R., Laman, H. & Tiedje, T. Optical absorption edge of semi-insulating GaAs and InP at high temperatures. *Appl. Phys. Lett.* **70**, 3540–3542 (1997).
 62. Ishizaka, F., Hiraya, Y., Tomioka, K., Motohisa, J. & Fukui, T. Growth of All-Wurtzite InP/AlInP Core-Multishell Nanowire Array. *Nano Lett.* **17**, 1350–1355 (2017).
 63. van Dam, D. *et al.* Directional and Polarized Emission from Nanowire Arrays. *Nano Lett.* **15**, 4557–4563 (2015).
 64. Gagliano, L. *et al.* Efficient green emission from wurtzite Al In P nanowires. 40–46 (2018). doi:10.1021/acs.nanolett.8b00621

65. Li, Q. & Wang, G. T. Spatial distribution of defect luminescence in GaN nanowires. *Nano Lett.* **10**, 1554–1558 (2010).
66. Xue, H. *et al.* Probing the strain effect on near band edge emission of a curved ZnO nanowire via spatially resolved cathodoluminescence. *Nanotechnology* **21**, (2010).
67. Pierret, A., Bougerol, C., Gayral, B., Kociak, M. & Daudin, B. Probing alloy composition gradient and nanometer-scale carrier localization in single AlGaIn nanowires by nanocathodoluminescence. *Nanotechnology* **24**, (2013).
68. Meuret, S. *et al.* Nanoscale Relative Emission Efficiency Mapping Using Cathodoluminescence g(2)Imaging. *Nano Lett.* **18**, 2288–2293 (2018).
69. Paggi, M., Berardone, I., Infuso, A. & Corrado, M. Fatigue degradation and electric recovery in Silicon solar cells embedded in photovoltaic modules. *Sci. Rep.* **4**, 1–7 (2014).
70. Degraaff, D., Lacerda, R., Campeau, Z. & Corp, S. Degradation mechanisms in Si module technologies observed in the field; their analysis and statistics. *NREL 2011 Photovolt. Modul. Reliab. Work.* 1–25 (2011).
71. Lindroos, J. & Savin, H. Review of light-induced degradation in crystalline silicon solar cells. *Sol. Energy Mater. Sol. Cells* **147**, 115–126 (2016).
72. Hashigami, H., Itakura, Y. & Saitoh, T. Effect of illumination conditions on Czochralski-grown silicon solar cell degradation. *J. Appl. Phys.* **93**, 4240–4245 (2003).
73. Yamaguchi, S. & Ohdaira, K. Degradation behavior of crystalline silicon solar cells in a cell-level potential-induced degradation test. *Sol. Energy* **155**, 739–744 (2017).
74. Bothe, K., Hezel, R. & Schmidt, J. Recombination-enhanced formation of the metastable boron-oxygen complex in crystalline silicon. *Appl. Phys. Lett.* **83**, 1125–1127 (2003).
75. Bothe, K., Sinton, R. & Schmidt, J. Fundamental boron-oxygen-related carrier lifetime limit in mono- And multicrystalline silicon. *Prog. Photovoltaics Res. Appl.* **13**, 287–296 (2005).
76. Wilking, S., Beckh, C., Ebert, S., Herguth, A. & Hahn, G. Influence of bound hydrogen states on BO-regeneration kinetics and consequences for high-speed regeneration processes. *Sol. Energy Mater. Sol. Cells* **131**, 2–8 (2014).
77. Bothe, K. & Schmidt, J. Electronically activated boron-oxygen-related recombination centers in crystalline silicon. *J. Appl. Phys.* **99**, (2006).
78. Glunz, S. W., Rein, S., Warta, W., Knobloch, J. & Wettling, W. Degradation of carrier lifetime in Cz silicon solar cells. *Sol. Energy Mater. Sol. Cells* **65**, 219–229 (2001).
79. Wilking, S. *et al.* Influence of hydrogen on the regeneration of boron-oxygen related defects in crystalline silicon. *J. Appl. Phys.* **194503**, 1–6 (2013).
80. Krugel, G., Wolke, W., Geilker, J., Rein, S. & Preu, R. Impact of hydrogen concentration on the regeneration of light induced degradation. *Energy Procedia* **8**, 47–51 (2011).
81. Tajima, M. Spectroscopy and topography of deep-level luminescence in photovoltaic silicon. *IEEE J. Photovoltaics* **4**, 1452–1458 (2014).
82. Reiche, M. & Kittler, M. Structure and properties of dislocations in silicon. *Cryst. Silicon - Prop. Uses* (2011).
83. Takahashi, Y. *et al.* Bragg x-ray ptychography of a silicon crystal: Visualization of the dislocation strain field and the production of a vortex beam. *Phys. Rev. B - Condens. Matter Mater. Phys.* **87**, 2–5 (2013).

ACKNOWLEDGEMENTS

And suddenly it is a year later, and the end of a fantastic adventure is in sight. During this adventure many people have helped me in a myriad of ways for which I will be forever grateful. Albert, thank you for letting me be part of your group and sharing your wisdom. Your gentle way of nudging us in the right direction by asking thought-provoking questions is unparalleled.

Sophie, it was an honour being your first master student and a pleasure to find and redefine our respective roles during the year. I tremendously enjoyed our frequent discussions and planning sessions and know that I will miss them wherever I end up. So thank you for being a fantastic supervisor and amazing person all-round.

Also many thanks to my office mates, Verena and (if we were lucky) Magda & Toon, and the other office clique of Nick, Tom, Andrea and Soren. Thank you for the fun lunches, discussion and revitalising coffee breaks. Also many thanks for helping me with my colloquium talk and your insights during group meetings. I hope to keep seeing many of you in the years to come.

I had the luck to also work with many people outside of my group during my project, and I would like to thank you for bearing with me. Harshel, your nanocubes were beautiful and helped me tremendously in my project, thank you for letting me use them. Andries and Hans, thank you for your help with the electron microscopy part. Luca, thank you for involving me in your NW project, I am really proud of the result. Also my collaborators for UNSW, Arestoo, Ziv, Michael, and Robbert it was an honour working with your various samples and a pleasure collaborating.

Besides my favourite research group, many other people at AMOLF contributed to making this year unforgettable. Since I do not expect any of them to actually read this, I will not waste paper with a long list of names. However, if you are reading this, chapeau :)

Finally, I would also like to thank all the people outside of AMOLF who provided me with moral support, laughs, and food during the times when the going was tough. My parents for always having my back and Alona for amplifying the joy in my life.

It was a beautiful year that I will cherish in my heart, thank you for sharing it with me.